STABILITY AND CONTROL OF FLAPPING FLIGHT: MODELING, SIMULATION, AND ANALYSIS

A Dissertation

Presented to the Faculty of the Graduate School

of Cornell University

in Partial Fulfillment of the Requirements for the Degree of

Doctor of Philosophy

by

Song Chang

August 2013

STABILITY AND CONTROL OF FLAPPING FLIGHT:

MODELING, SIMULATION, AND ANALYSIS

Song Chang, Ph.D.

Cornell University 2013

We study the stability and control of flapping flight of insects. To quantify the stability and to assess the control, we build a 3D dynamic flight model, which takes into account the instantaneous coupling between the insect body and the wings. To compare with published results, we also implement a time-averaged model where aerodynamic forces are averaged over every wing-beat. To stabilize hovering flight, we design a control algorithm that incorporates a discrete sampling and a time delay within neural feedback circuits. Our study suggests conditions that the sampling interval and the delay time should satisfy so as to actively stabilize flapping flight. We also investigate how passive stability can be achieved for flapping flight by tuning wing attachment points. Finally, we extend our stability analysis and controller design to ascending flight.

BIOGRAPHICAL SKETCH

The author of this thesis, Song Chang, was born in the People's Republic of China in 1983. Song Chang studied in the School of Physics at Peking University from 2002 to 2006. In 2006, Song Chang obtained a Bachelor of Science with honors from Peking University. Song Chang continued his study in the Graduate School at Cornell University and majored in the field of Applied Physics. In 2010, Song Chang obtained a Master of Science from Cornell University. Till the time when this thesis was written, Song Chang has been working on theoretical problems related to the interaction between objects and their surrounding fluid, such as the flapping flight of insects and the free fall of seeds in the air.

Dedicated to my beloved parents,

Li-bin Chang and Zhi-min Song

ACKNOWLEDGEMENTS

During the years of study at Cornell University, I benefited from by my interaction with people from a variety of backgrounds.

I would like to first thank my advisor, Professor Zheng Jane Wang, for all her advice during the past five years. Her guidance has expedited the development of my professionalism, as well as my adaptation to a new country and new culture. Not only have I gleaned an enormous amount of brilliant thoughts from her, I have also learned from her how to think critically and how to conduct scientific research.

I would like to thank the other two members on my special committee, Professor John Mark Guckenheimer and Professor Itai Cohen. The regular discussions I had with them provided me with valuable help to my research. It was always exciting when I began thinking more actively and effectively about the problems at hand, simply after having a chat with the professors. I thank Professor Guckenheimer in particular for his advice on my minor degree in applied mathematics.

I would like to thank several professors, graduate students, and friends, with whom I have discussed research and/or life-related issues. These include Professor J. T. Gene Hwang, Professor Zhigen Zhao, Professor Andy Ruina, Dr. Attila Bergou, Dr. Leif Ristroph, Dr. Gordon Berman, Kevin Chen, Lei Huang, James Melfi, Michael Weiner, and a long list of others not mentioned here. I thank all those who I have not included, but who have beneficially influenced my progress in both academic and personal senses.

I thank the National Science Foundation for supporting my research and the School of Mathematics at Cornell University for offering me teaching positions. This thesis would not exist if not for these two sources of financial aid.

Lastly, but definitely not the least, I want to thank my dear parents for their consistent understanding and love.

TABLE OF CONTENTS

LIST OF TABLES

LIST OF FIGURES

CHAPTER 1

Overview

Flapping flight is intrinsically unstable. Without active control, insect-scaled robotic fliers cannot hover stably but tumble and descend [1]. Similar instability is also observed in numerical simulations of flapping flight [2, 3]. On the other hand, fruit flies are equipped with mechanosensory organs, the halteres, to sense their body rotation [4] and rely on neural feedback control to stabilize their flight and to execute turning maneuvers. When halteres are disabled, fruit flies exhibit unstable flight similar to that observed in uncontrolled robots [4, 5].

It is challenging to decipher the neural feedback control utilized by flying insects, based on recordings of their flight trajectories and wing stroke patterns [4–14]. There are numerous questions to answer about the neural control used by insects to stabilize flight. How do insects modulate their wing strokes to correct their flight course? What kind of neural computations and muscle activities are involved in the feedback control? How often and how fast do insects have to adjust their wing strokes to remain stable? What kind of theoretical limits are imposed on the time scales in the feedback control by both neurophysiology and by the dynamics of flapping flight? These questions and the related studies have motivated our research.

Two kinds of approaches are used to answer these questions, the experimental approach and the computational approach. In experiments, one studies the response of insects to stimuli or perturbations and the associated modulations of wing stroke patterns. Correlations between flight dynamics and wing modulations have been studied in the response of tethered insects to visual stimuli [6, 15–18], in observations of free flight [7, 19–21], and in recent three-dimensional tracking of free flight [5, 12–14, 22–26]. Beyond understanding the correlations between the wing motion and the body motion,

the experimenters also have to inspect the mechanism by which the wing modulations lead to changes in body dynamics, which entails dynamic modeling and analysis. The mechanism may provide clues to designing control schemes to stabilize flight or to exert specific turns [27].

In computer simulations, one analyzes the stability and control of an insect model. Recent studies have analyzed flight stability in both longitudinal flight [2, 28, 29] and lateral flight [30, 31]. In these studies, the stability of flapping flight can be related to that of fixed-wing airplanes [32], provided that the frequency of wing-beat is much greater than that of body oscillations [3]. In such a limit of fast wing-beat frequency, the aerodynamic forces can be approximated by their time-averaged values over a wing-beat cycle. The governing equations for body dynamics near equilibrium flight can be further simplified into a set of linear equations [2, 3, 33]. For longitudinal flight, the primary instability is associated with the body-pitch dynamics, resulting from the dynamic coupling between the forward motion and the pitch motion of the body. This instability is recognized by linear stability analysis in both time-averaged models [2] and in numerical simulations where the instantaneous coupling between the body and the wings is taken into account [34]. In addition to the stability analysis, classical control theory can predict the controllability of the averaged dynamics in the linear regime [35]. A natural question is how the instability of flapping flight behaves in a nonlinear regime, where the instantaneous coupling between the body and the wings is considered.

In this work, we would like to address the following questions. (1) How can we study the stability and control of flapping flight in such a nonlinear regime where we take into account the instantaneous wing-body coupling? (2) How can we design a controller to stabilize hovering flight in the nonlinear regime, where classical control theory no longer applies? (3) How can we design robotic fliers with flapping wings whose flight

is passively stable? (4) How can the stability and control of hovering flight be adapted to different flight modes, such as ascending flight?

Answers to those questions may provide clues to both the internal control schemes utilized by flying insects and control strategies applicable to robotic fliers. To quantify the stability and investigate the controllability of free flight, we need a computational tool that can simulate flapping flight in both open-loop and closed-loop conditions. However, few results have been published on dynamic stability and control in this nonlinear regime of flapping flight. As a result, we build a dynamic model that takes into account the instantaneous coupling, with which we analyze the stability and investigate the control of flapping flight. We also implement a time-averaged model of flapping flight to compare the results.

Here we lay out the plan for the following chapters:

In chapter 2, we describe our methods of simulating free flapping flight, using a model we call the "3D dynamic flight model". The model treats flapping flight as a coupled rigid body motion and takes into account the instantaneous coupling. We enumerate the ingredients of the model: rigid body dynamics, quasi-steady aerodynamics, a prescribed wing motion, and parameters for fruit flies. We also explain the importance of considering this instantaneous wing-body coupling.

In chapter 3, we design a discrete-sampling, time-delayed, linear controller for body-pitch in longitudinal flight. The controller includes three important time scales: a sampling interval, a sensory delay, and an actuation delay. We study the effectiveness of the controller with different combinations of sampling interval and sensory delay and determine conditions on the two time scales for effective control. The results lead us to conjecture that fruit flies sense their body kinematics every wing-beat and take control

actions with a delay of two wing-beats. We discuss the plausibility of such a beat-to-beat control, based on findings in neural studies of flies.

In chapter 4, we study how changes of wing attachment points affect the stability of hovering. We implement a second model of free flight, which we call the "time-averaged model". Using both models, we test whether passive stability can be achieved in hovering and compare the results.

In chapter 5, we study stability and control for ascending flight. We employ the same controller designed for hovering and investigate its performance under different ascending speeds.

CHAPTER 2

3D Dynamic Flight Model[1]

In this chapter, we describe the first model we build for flapping flight, which we call the 3D dynamic flight model. The model approximates the insect body and the wings by rigid bodies and simulates flapping flight as interconnected rigid body motion. The wing motions are prescribed with respect to the insect body, and we solve for the motion of the insect body, subject to aerodynamic forces and torques applied on the insect wings.

In our simulation, the motion of each rigid body is governed by physical laws and constrained by its connection to other rigid bodies. Methods of treating coupled rigid body dynamics include Lagrangian mechanics that treats the constraints implicitly [36], methods that rely on the principle of virtual work [37], and black-box solvers popular among game developers [38]. Here we treat constraints in our problem explicitly by incorporating unknown constraint forces and torques. This treatment is similar to that in [39]. In addition to dynamic equations for each rigid body, we include constraint equations into our model, based on prescribed wing motions and the connections among the rigid bodies. By combining the dynamic equations and the constraint equations, we are able to solve for unknown accelerations of the rigid bodies and the constraint forces and torques. The kinematics of the insect body are evolved in the state space, according to the solved accelerations.

Our algorithm of rigid body dynamics takes into account instantaneous coupling between the insect body and the wings. This is different from most of previous studies, which mainly rely on time-averaged aerodynamic forces and torques in their dynamic modeling [2, 3, 28, 33, 35]. Those studies concern the linear stability of insects at hover-

[1]This chapter is from a paper, "Insects in Free Flight: Simulation, Dynamic Instability, and a Prediction for the Critical Sensing Rate for Flight Stabilization", by the author and Z. Jane Wang. The paper has been submitted to PNAS [60].

ing, and thus a time-averaged treatment suffices, provided that the wing-beat frequency in their models is much higher than typical frequencies of flight modes. In our study of flight control, however, we design a controller that can sense body kinematics within a wing-beat (chapter 3). Thus, our dynamic modeling needs to consider the body oscillation due to the periodic wing-beats. Furthermore, we notice that oscillation of body attitude within each wing-beat can lead to observable dynamic effect. A large oscillation amplitude may reduce the mean vertical lift and cause the insect to descend, whereas a small oscillation amplitude leads to a hovering flight (chapter 4). This phenomenon is not captured by the time-averaged models, which simply assume an underlying hovering flight. We thus deem this instantaneous coupling as an important element in our 3D dynamic flight model. Compared to previous research that also considers the instantaneous coupling [34], our physical equations and mathematical derivations are conceptually simpler.

Computational fluid dynamics are used in research of flapping flight to compute aerodynamic forces and torques [2]. Our study requires extensive simulations within the space of model parameters, and each simulation corresponds to a flight of several hundred wing-beats. As a result, we adopt a quasi-steady aerodynamic model that is more computational efficient.

To study flight of fruit flies and to compare with experimental results, we prescribe the wing motion in our model so that it mimics the wing stroke pattern of fruit flies. The model parameters are set for fruit flies. In the following sections, we elaborate our algorithm for rigid body dynamics, the quasi-steady aerodynamic model, the prescribed wing motion, as well as parameters in the model.

2.1 Modeling and Simulation Methods

Our insect model consists of $(n + 1)$ rigid bodies, an insect body and n wings. Each wing is modeled as an ellipsoid connected to the insect body through a ball joint. Each joint allows for three degrees of freedom in rotation. In our model, the wing motion is prescribed relative to the insect body. To compare with experimental findings, the wing motion in our model mimics a figure-8 wing stroke pattern that is usually observed in fruit flies. After the wing motion is determined, we solve for the body motion with coupled rigid body dynamics.

To simulate 3D free flapping flight, we solve Newton-Euler equations for the coupled wing-body system. Our method for simulating the flight dynamics is based on the idea that the coupling among rigid bodies can be handled through constraint forces and torques. These constraint forces and torques are unknown at each instant, but are solved from a linear equation system consisting of dynamic equations and constraint equations.

2.1.1 Insect Body Dynamics

Dynamics of the insect body are governed by the gravity and the constraint forces and torques. In the model, we take a convention that constraint forces and torques are applied upon the wings by the insect body. As a result, the insect body experiences reactions. The governing equations for the insect body dynamics are

$$m^b \vec{a}^{\,b} = m^b \vec{g}^{\,b} - \sum_{i=1}^{n} \vec{f}_i^{\,c} \tag{2.1}$$

$$\mathbf{I}^b \vec{\beta}^{\,b} = -\vec{\omega}^{\,b} \times (\mathbf{I}^b \vec{\omega}^{\,b}) - \sum_{i=1}^{n} \vec{\tau}_i^{\,c} - \sum_{i=1}^{n} \vec{r}_i^{\,b} \times \vec{f}_i^{\,c}, \tag{2.2}$$

where b denotes the insect body, m is the mass, $\mathbf{I}$ is the moment of inertia tensor, $\vec{a}$ is the linear acceleration, $\vec{\beta}$ is the angular acceleration, $\vec{g}$ is the gravitational vector, $\vec{\omega}$ is the

angular velocity, $\vec{f}^{\,c}$ and $\vec{\tau}^{\,c}$ are the constraint force and torque, respectively, and $\vec{r}_i^{\,b}$ is the position of the *i*-th wing-root relative to the body center of mass. The first equation is Newton's equation, in which body acceleration is proportional to the total force, i.e. the sum of gravity and reactions of all constraint forces. The second equation is Euler's equation for rigid body rotation, where the tensor product of the moment of inertia and the angular acceleration equals the total torque, i.e. the sum of constraint torques and torques due to constraint forces. In Euler's equation, the cross term on the right side is due to a conventional choice of decomposing the angular velocity within the co-rotating body frame. In the equations, we have neglected aerodynamic forces and torques on the insect body.

2.1.2 Wing Dynamics

The dynamics of the wings are similar to those of the insect body, except that aerodynamic forces and torques are applied on the wings. The governing equations for the dynamics of each wing are

$$m_i^w \vec{a}_i^{\,w} = m_i^w g + \vec{f}_i^{\,c} + \vec{f}_i^{\,a} \tag{2.3}$$

$$\mathbf{I}_i^w \vec{\beta}_i^{\,w} = -\vec{\omega}_i^{\,w} \times \mathbf{I}_i^w \vec{\omega}_i^{\,w} + \vec{\tau}_i^{\,c} + \vec{r}_i^{\,w} \times \vec{f}_i^{\,c} + \vec{\tau}_i^{\,a}, \tag{2.4}$$

where *w* denotes the wing, $\vec{r}_i^{\,w}$ is the position of the wing-root relative to the center of mass of the *i*-th wing, and $\vec{f}_i^{\,a}$ and $\vec{\tau}_i^{\,a}$ are, respectively, the aerodynamic force and torque on the *i*-th wing. Compared to the dynamic equations for insect body, the wing dynamics are governed by the same set of equations with additional aerodynamic terms.

2.1.3 Dynamic Constraints

There are two types of constraints applied at each joint connecting a wing and the insect body. The first type is due our prescription of the wing motion. At each instant, the angular acceleration of a wing, $\vec{\beta}_i^{\,w}$, is not independent of the angular acceleration of the insect body, $\vec{\beta}^{\,b}$. The two angular accelerations are correlated, and their relationship is expressed in the following equation,

$$\vec{\beta}_i^{\,r} = \vec{\beta}_i^{\,w} - \vec{\beta}^{\,b} \tag{2.5}$$

Physically, the relative angular acceleration of each wing with respect to the insect body is constrained to agree with the prescribed motion, $\vec{\beta}_i^{\,r}$.

The second type of constraint equations is due to the fact that each wing is constantly connected to the insect body at a given joint, the wing attachment point. At each wing attachment point, we may calculate its instantaneous linear acceleration based on either the kinematics of the insect body or the kinematics of the wing. The calculation should be the same, regardless of which kinematics we use. As a result,

$$\vec{a}^{\,b} + \vec{\beta}^{\,b} \times \vec{r}_i^{\,b} + \vec{\omega}^{\,b} \times \vec{\omega}^{\,b} \times \vec{r}_i^{\,b} = \vec{a}_i^{\,w} + \vec{\beta}_i^{\,w} \times \vec{r}_i^{\,w} + \vec{\omega}_i^{\,w} \times \vec{\omega}_i^{\,w} \times \vec{r}_i^{\,w} \,. \tag{2.6}$$

Adding this equation to the model guarantees the wing-body connection at the joint all the time.

2.1.4 Kinematic Evolution

We have so far involved $(4n + 2)$ unknown vectors, $\vec{a}^{\,b}$, $\vec{\beta}^{\,b}$, $\vec{a}_i^{\,w}$'s, $\vec{\beta}_i^{\,w}$'s, $\vec{f}_i^{\,c}$'s, $\vec{\tau}_i^{\,c}$'s, in our model equations. Those unknown vectors are solved by the above $(4n + 2)$ vectorial equations, which are linear in the unknowns. In an example of a two-winged insect,

such as a fruit fly, $n = 2$, and the linear system has a dimension of 30. Once the unknown linear and angular accelerations are solved, they are used to evolve the insect body kinematics in state space.

The insect body kinematics are given by its position $\vec{r}^{\,b}$, linear velocity $\vec{v}^{\,b}$, Euler angles ϕ^b,θ^b,η^b, and angular velocity $\vec{\omega}^{\,b}$. We adopt the XYZ convention in our definition of Euler angles: a first yaw angle, ϕ^b, about the vertical axis, followed by a body-pitch angle, θ^b, between the body longitudinal axis and the vertical axis, and a last roll angle, η^b, about the body longitudinal axis (Figure 2.1). After solving for the insect body accelerations, $\vec{a}^{\,b}$ and $\vec{\beta}^{\,b}$, the body kinematics are evolved in the state space, according to

$$\dot{\vec{r}}^{\,b} = \vec{v}^{\,b} \tag{2.7}$$

$$\dot{\vec{v}}^{\,b} = \vec{a}^{\,b} - \vec{\omega}^{\,b} \times \vec{v}^{\,b} \tag{2.8}$$

$$\dot{\phi}^b = \left(\omega_y^b \sin\eta^b + \omega_z^b \cos\eta^b\right) / \cos\theta^b \tag{2.9}$$

$$\dot{\theta}^b = \omega_y^b \cos\eta^b - \omega_z^b \sin\eta^b \tag{2.10}$$

$$\dot{\eta}^b = \omega_x^b + (\sin\theta^b)\dot{\phi}^b \tag{2.11}$$

$$\dot{\vec{\omega}}^{\,b} = \vec{\beta}^b. \tag{2.12}$$

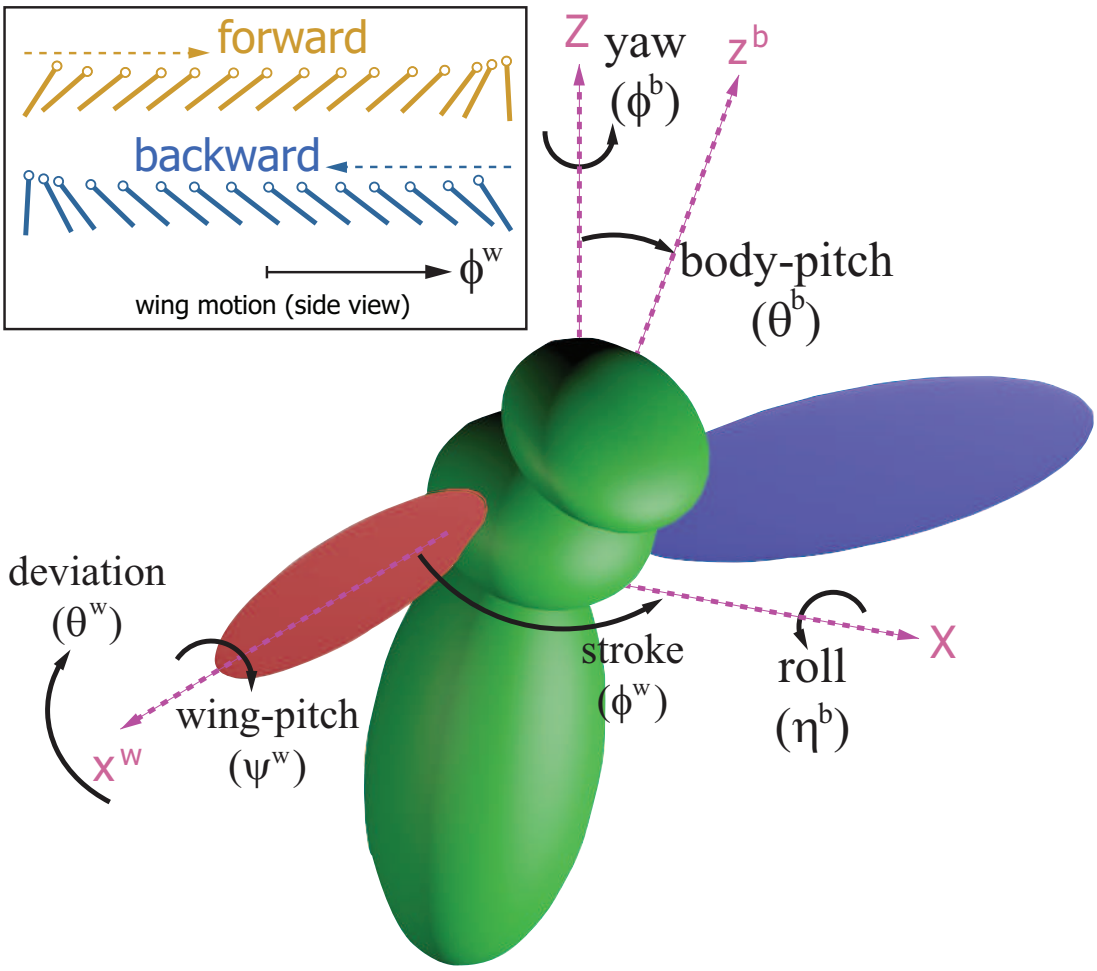

Figure 2.1: Model fruit fly. In longitudinal flight, the body has 3 degrees of freedom : translations in the vertical plane and body-pitch rotation, θ^b. Each wing is connected to the body through a ball joint and has 3 rotational degrees of freedom, specified by three Euler angles in the XYZ convention. (Inset) Side view of wing stroke pattern.

2.2 Quasi-steady Aerodynamics

Because our research involves extended simulations for both dynamic stability calculations and control analyses, we adopt a quasi-steady aerodynamic model in our computation. This quasi-steady model was originally derived for 2D falling plates in fluid [40, 41]. The model precision was tested by comparing forces and torques generated by the quasi-steady model with those measured from experiments on free falling plates [42]. We invoke a blade element approximation and use the quasi-steady model to compute the aerodynamic force and torque on each blade. In our model, a blade is a thin stripe of the wing that is sliced in the local chord direction. The total aerodynamic force and torque on each wing is an integration of the blade element contributions along local span direction.

The quasi-steady aerodynamic model includes a circulatory lift ($\vec{f_L}$), a dissipative drag ($\vec{f_D}$), a damping torque ($\vec{\tau}_D$), and force and torque due to added mass effect ($\vec{f_A}, \vec{\tau}_A$). We take the wing span direction as the local x-axis.

2.2.1 Circulatory Lift

On each blade, the lift due to the circulation is

$$\vec{f_L} = -\rho_f \vec{\Gamma}(s) \times \vec{v}(s), \tag{2.13}$$

where ρ_f is the air density, $\vec{v}(s)$ is the translational velocity within the local y-z plane of the blade at span-wise locations s, and $\vec{\Gamma}(s) = \left(2C_R\, c(s)^2 \omega(s) - C_T\, c(s) \sin 2\alpha(s)\right) \hat{x}$ is the aerodynamic circulation in the local x direction. Here $c(s)$ is the chord length of the blade, $\omega(s)$ is the rotational velocity about the local x axis, $\alpha(s)$ is the geometric angle of attack, and C_T and C_R are constant coefficients.

2.2.2 Dissipative Drag

The dissipative drag,

$$\vec{f}_D = -\rho_f \kappa(s)\vec{v}(s)\,, \tag{2.14}$$

opposes the local translational velocity, and the resistivity is given by $\kappa(s) = c(s)[A - B\cos 2\alpha(s)]v(s)$, where A and B are parameters.

2.2.3 Damping Torque

The damping torque,

$$\vec{\tau}_D = -\rho_f \lambda(s)\vec{\omega}(s)\,, \tag{2.15}$$

opposes the local rotational velocity, and the rotational resistivity is given by $\lambda(s) = \pi\rho_f c(s)^4(\mu_1\frac{U}{L} + \mu_2|\omega(s)|)$.

2.2.4 Associated Torques

The center of pressure is shifted from the center of mass. Corresponding to the circulatory lift and the dissipative drag, force moments are calculated about the wing center of mass,

$$\vec{\tau}_f = \vec{s}\times\left(\vec{f}_L + \vec{f}_D\right). \tag{2.16}$$

2.2.5 Added Mass Effect

In addition to the aerodynamic components listed above, we consider the force and torque due to added-mass effect. The added mass force is

$$\vec{f_A} = [-m_{33} v_z \omega_y, m_{33} v_z \omega_x, -m_{33} \dot{v}_z]^T , \tag{2.17}$$

and the torque is

$$\vec{\tau}_A = \begin{bmatrix} -m_{44}\dot{\omega}_x + m_{55}\omega_z\omega_y - m_{33}v_y v_z \\ -m_{55}\dot{\omega}_y - m_{44}\omega_z\omega_x + m_{33}v_x v_z \\ (m_{44} - m_{55})\omega_x\omega_y \end{bmatrix} , \tag{2.18}$$

where m_{33}, m_{44}, m_{55} are constant added-masses [43, 44].

2.2.6 Total Aerodynamics

The total aerodynamic force and torque upon each wing are, respectively,

$$\vec{f}^a = \vec{f_L} + \vec{f_D} + \vec{f_A} \tag{2.19}$$

$$\vec{\tau}^a = \vec{\tau}_f + \vec{\tau}_D + \vec{\tau}_A . \tag{2.20}$$

2.3 Prescribed Wing Motions

The wing motion is described by three rotational angles: $\phi(t)$, the stroke angle, $\theta(t)$, the deviation angle, and $\psi(t)$, the wing-pitch angle (Figure 2.1). To model the wing motions representative of fruit flies, we use the form suggested in [45],

$$\phi(t) = \phi_0 + \phi_m \frac{\arcsin[K \sin(2\pi f t)]}{\arcsin K} \tag{2.21}$$

$$\theta(t) = \theta_0 + \theta_m \cos(N \cdot 2\pi f t + \delta_\theta) \quad (2.22)$$

$$\psi(t) = \psi_0 + \psi_m \frac{\tanh[C \sin(2\pi f t + \delta_\psi)]}{\tanh C}, \quad (2.23)$$

where ϕ_0, θ_0, ψ_0 are the constant offsets, ϕ_m, θ_m, ψ_m are amplitudes, f is the wing-beat frequency, δ_θ and δ_ψ are the phase shifts, and N,K,and$C$ are three waveform parameters. $N = 1$ or 2. $N = 1$ corresponds to one vertical oscillation per stroke, and $N = 2$ corresponds to a figure-8 motion. $0 < K < 1$. ϕ becomes sinusoidal when K is close to 0 and triangular when K close to 1. $C > 0$. ψ becomes sinusoidal for small C and a step function for large C. Figure 2.1 shows the wing Euler angles used in our simulation.

2.4 Parameters in Model

We use the morphological parameters similar to those for fruit flies, *Drosophila melanogaster* [5, 23]: body weight = 1.1 mg, body length = 2.4 mm, maximum body cross-section = 1.2mm ×1.2 mm, wing weight = 3.6×10^{-3} mg, wing span = 2 mm, maximal wing chord = 1 mm, maximal wing thickness = 0.1 mm. We use the following parameters in modeling the wing motion during uncontrolled flight: $f = 250$Hz, $\phi_m = 63^\circ$, $\phi_0 = 0^\circ$, $K = 0.7$, $\theta_m = \theta_0 = 0^\circ$, $\psi_m = 53^\circ$, $\psi_0 = 90^\circ$, $\delta_\psi = -72.4^\circ$, and $C_\psi = 2.4$. For simplicity, we have neglected the deviation from the mean stroke plane, and we select the phase shift in $\psi(t)$ so that the wing pitches in advance of the wing stroke reversal. The wing stroke amplitude is estimated so that the mean aerodynamic lift roughly balances the body weight. In this work, we use symmetric wing beats on both wings to study the longitudinal flights. We use the following parameters in the quasi-steady aerodynamic model: $C_T = 1.5$, $C_R = \pi$, $A = 1.4$, $B = 1$, $\mu_1 = 0.2$, $\mu_2 = 0.2$, $m_{33} = 1.1 \times 10^{-3}$mg, $m_{44} = 3.2 \times 10^{-7}$ mg·mm^2, and $m_{55} = 3.1 \times 10^{-5}$ mg·mm^2.

2.5 Summary

In this section, we described one of our models of flapping flight, the 3D dynamic flight model. The model treated flapping flight as a coupled rigid body motion, with the insect body and the wings approximated as rigid bodies. This model took into account the instantaneous coupling between the insect body and the wings. The instantaneous coupling is an important element in our model.

We dealt with the constraints in our simulation by including the unknown constraint forces and torques. We listed the dynamic equations and the constraint equations in our model. These equations were used to solve for the unknown accelerations and the unknown constraint forces and torques. The solved accelerations of the insect body are used to evolve the body kinematics in the state space.

We employed a quasi-steady aerodynamic model for computing the aerodynamic forces and torques on the wings. This enabled us to run extensive simulations. We prescribed the wing motion to mimic the wing stroke pattern of fruit flies. We set model parameters for fruit flies.

CHAPTER 3

Body-pitch Control in Hovering Flight[1]

Flapping flight is intrinsically unstable [2, 29], and thus the stable flight of fruit flies can only be a result of active control. In this chapter, we first examine simulated flight trajectory when the wing motion is not modulated by feedback control. From our examination of the flight trajectory, we infer general characteristics of uncontrolled flapping flight and the instability in body-pitch.

We then describe how we design and implement a discrete-sampling, time-delayed, linear controller, which compensates for the body-pitch instability and stabilizes flapping flight. The controller modulates the center position of the periodic wing stroke, based on measured body-pitch attitude and rotational velocity. Such a control scheme was observed in the flight of fruit flights in experiments [18, 19]. When designing the controller, we consider three important time scales: a sampling interval, a sensory delay, and an actuation delay. After we implement the control algorithm in our dynamic flight model, we demonstrate a body-pitch stabilization in a simulation of hovering flight.

Among the three control time scales, the actuation delay depends on mechanical properties of the wing hinges and the steering muscles at wing-roots. On the other hand, the other two control time scales, the sampling interval and the sensory delay, are directly related to the neural feedback control loop and reflect fundamental physical constraints faced by flying insects. Thus, we study the controller performance for different combinations of the sampling interval and the sensory delay and identify a set of combinations of the two time scales that corresponds to well-controlled flight. The region of those combinations suggests a range of critical time scales for the body-pitch

[1]This chapter is from a paper, “Insects in Free Flight: Simulation, Dynamic Instability, and a Prediction for the Critical Sensing Rate for Flight Stabilization”, by the author and Z. Jane Wang. The paper has been submitted to PNAS [60].

control. Combining experimental findings of reaction time of fruit flies, we refine the boundary on the sampling interval and the sensory delay. Lastly, based on controller's robustness, we conjecture that fruit flies sense their body kinematics every wing-beat and execute control commands with a time delay around two wing-beats. We finish the chapter with a discussion of whether a sampling interval of one wing-beat is plausible, given our knowledge of fruit flies' steering muscles.

3.1 Simulation of Uncontrolled Flapping Flight

With the model insect initially at rest ($u = v = \omega = 0$) and upright ($\theta = 0$), we simulate its flight with the periodic wing motion. A typical trajectory consists of three phases. The first four segments in Figure 3.1 correspond to an initial nose down-and-up oscillations in the body-pitch. During the first 10 wing-beats, the aerodynamic torque pitches the body nose-down ($A \to B$). Thus, the aerodynamic lift tilts forward and drives the insect forward ($B \to C$). The forward motion couples with the back-and-forth wing motion and results in a drag that pitches the body up ($C \to D$). The drag and the horizontal component of the lift decelerate the body, and the body eventually moves backwards ($D \to E$). The backward motion is coupled with the wing motion to produce a nose-down torque ($E \to F$). The body pitch oscillates as a result of this coupling between the horizontal and the body-pitch motions, which is consistent with the general picture in the averaged-dynamic model [3]. The amplitude of the oscillation increases, and the body accelerates in descent.

After a transient (panel E), the body reaches a steady descent with a terminal speed around 50 cm/s and a body oscillation amplitude $\sim 48^\circ$. Because of the body-pitch oscillation, the mean vertical lift due to flapping motion is smaller than the body weight, and the weight balance requires a significant descent velocity to induce a vertical drag

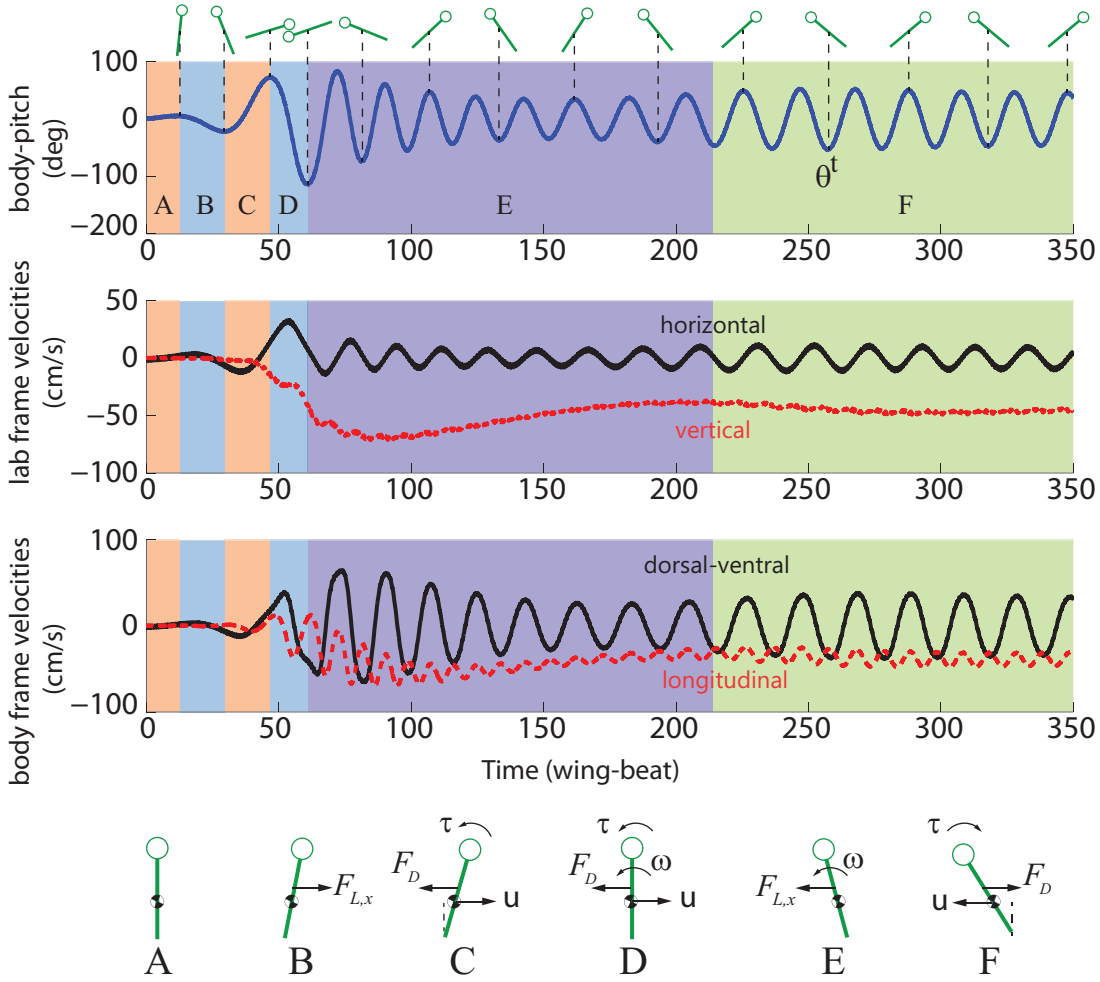

Figure 3.1: Uncontrolled flight kinematics. Body-pitch (top) and translational velocities in laboratory (middle) and in the body frame (bottom). The horizontal velocity is 90° phase shifted from the body-pitch oscillation. The bottom schematic shows the mechanism for pitching instability due to the coupling between the forward translation and the body-pitch rotation.

force. It is also worth noting that the oscillation period of 20 wing-beats is comparable to the inherent time scale of the insect body taken as a compound pendulum. In the body frame, the velocity component along the longitudinal axis oscillates twice as fast as does the component along the dorsal-ventral axis, consistent with the ratio between the frequencies of the driving forces along those directions. All the oscillations are in phase.

Without a stabilization algorithm, the insect does not fly erratically, but reaches a steady state tumbling descent. In this case, the body weight is largely balanced by a vertical drag due to the coupling between the descending velocity and the wing motion. We have varied the model parameters, including the geometry and inertia of both wing and body, as well as the wing attachment, and find similar steady states.

3.2 Discrete-sampling, Time-delayed, Linear Controller for Body-pitch

The coupling between the forward motion and the body-pitch rotation described above is the primary cause of the instability of longitudinal flight. To control the body pitch, the insect must generate a corrective torque. Insects are equipped with various sensory systems to measure their self-kinematics, and control decisions can be made based on the measurements [11]. A fruit fly can correct its body-pitch by modulating the center position of the wing stroke [7, 18, 19]. The center position is shifted forward to correct a nose-down perturbation and backward to correct a nose-up perturbation.

Based on this strategy, we construct a controller that adjusts the center of the wing stroke (Figure 3.2(a)) according to the body-pitch and body-pitching rate measured

at a previous time. When designing the control algorithm, we take into account two features of a mechanosensory system. First, the biological control is likely to operate at discrete time intervals in sensing and actuation, given discrete spikes of neuron firings. Second, there is a finite time delay from sensing to actuation, which reflects the fundamental neurophysiological constraint in biological control pathways [5, 13, 46]. A generic discrete-sampling, time-delayed, linear controller has the form, $\phi_0(t) = k_u u(t-\tau) + k_v v(t-\tau) + k_\theta \theta(t-\tau) + k_\omega \omega(t-\tau)$, which modulates the center position of the wing stroke at discrete intervals proportional to the perturbation in body kinematics. Here u, v, θ, ω are the perturbed kinematics, $k_u, k_v, k_\theta, k_\omega$ are the controller gains, and τ is the delay time. In this paper, we study the feedback control involving the halteres that sense the body rotation, and we set $k_u = k_v = 0$. In essence, the controller is a proportional-integral control, with ω the directly sensed variable by the mechanosensory organ (e.g. the haltere [4]) and θ its integration in time. We focus on the effect of the sampling interval and reaction delay on the controller performance.

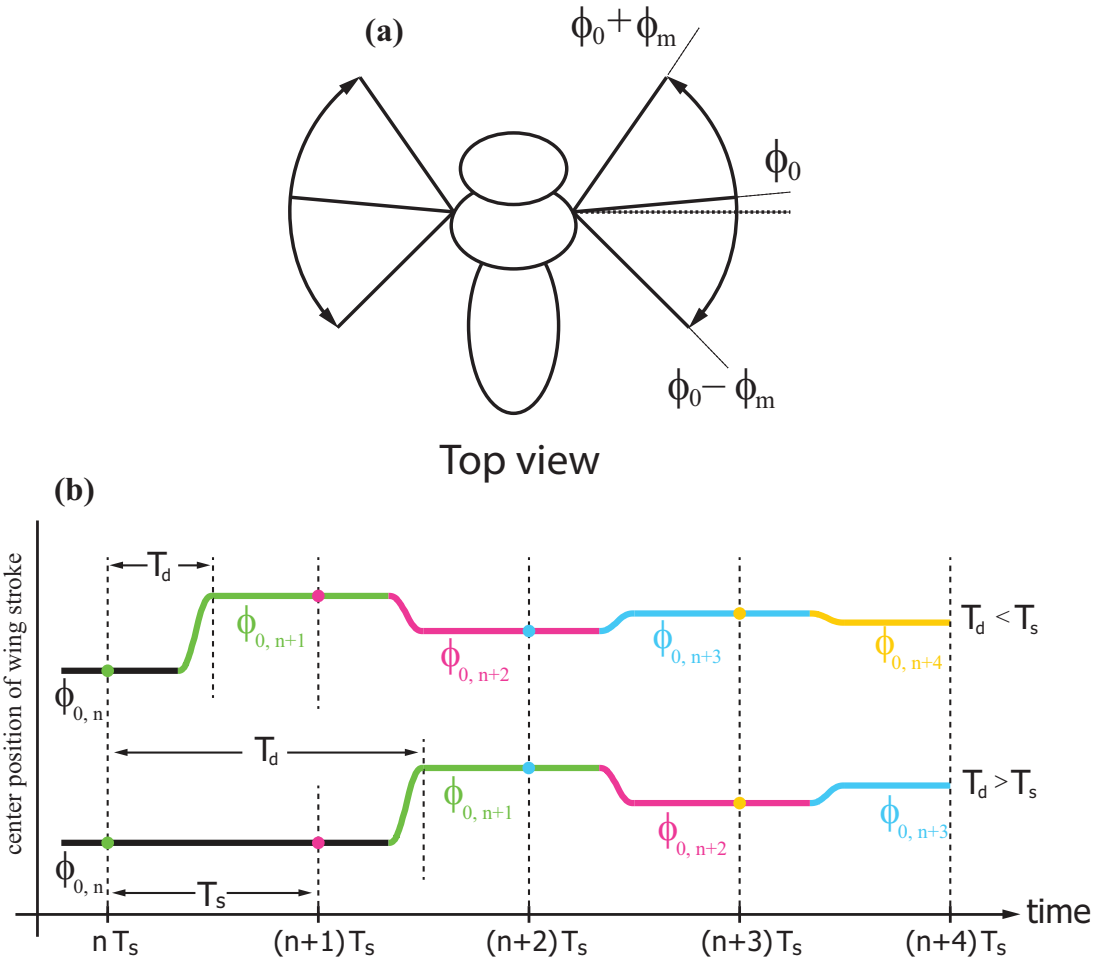

Figure 3.2: (a) Body-pitch controlled by center position of wing stroke, ϕ_0. (b) Two sample sequences of control actions in our proposed controller. The insect samples with a sampling period, T_s, and acts with a delay, T_d, to adjust ϕ_0.

Figure 3.2(b) illustrates the sequence of events in our controller. At the beginning of a sampling interval, T_s, the insect senses its body kinematics. The control algorithm computes the shift of the center position of the wing stroke, $\Delta\phi_0 = \phi_{0,n+1} - \phi_{0,n}$, which takes a time interval of T_d to execute. The transition from $\phi_{0,n}$ to $\phi_{0,n+1}$ consists of an initially quiescent period of $T_{d,1}$ mimicking the reaction time and a ramp-up period of $T_{d,2}$ mimicking the actuation. The actuation is modeled by a function,

$$\phi_0(\hat{t}) = \phi_{0,n} + (\phi_{0,n+1} - \phi_{0,n})(10\hat{t}^3 - 15\hat{t}^4 + 6\hat{t}^5), \tag{3.1}$$

where $\hat{t} = (t - t_n - T_{d,1})/T_{d,2}$, $(0 \le \hat{t} \le 1)$ is the rescaled time variable and t_n is the time at the n-th measurement. The polynomial function, $10\hat{t}^3 - 15\hat{t}^4 + 6\hat{t}^5$, corresponds to a transition between two binary levels 0 and 1, and the curve is 2nd order differentiable at both endpoints of its domain (Figure 3.3).

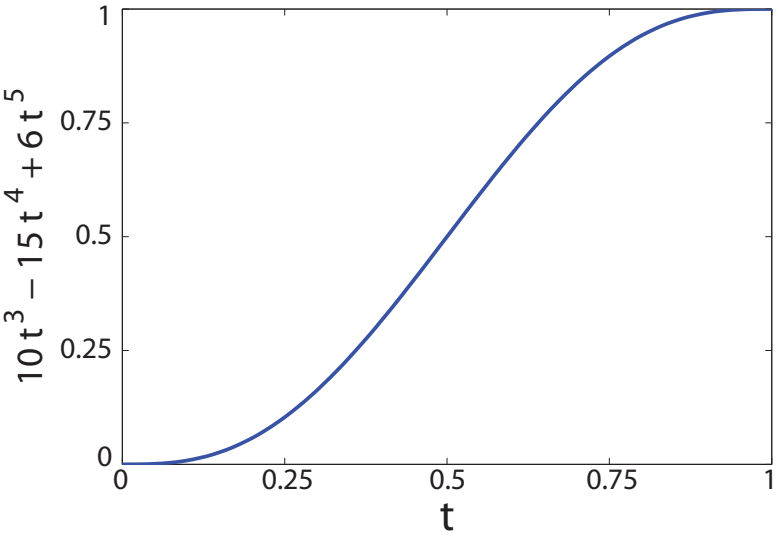

Figure 3.3: A smooth transition from 0 to 1, when the independent variable changes from 0 to 1. The curve is second order differentiable at both ends.

3.3 Simulation of Stabilized Hovering Flight

Figure 3.4 displays the body-pitch in a controlled longitudinal flight with $k_\theta = 0.206$, $k_\omega = 0.005$, $T_s = 1$ and $T_d = 2.2$, in comparison with the simulation from uncontrolled flight. With the control, the body-pitch gradually settles down to an undulating steady state with the same frequency as the wing motion. The control command converges to a constant, which is small compared to the wing stroke amplitude.

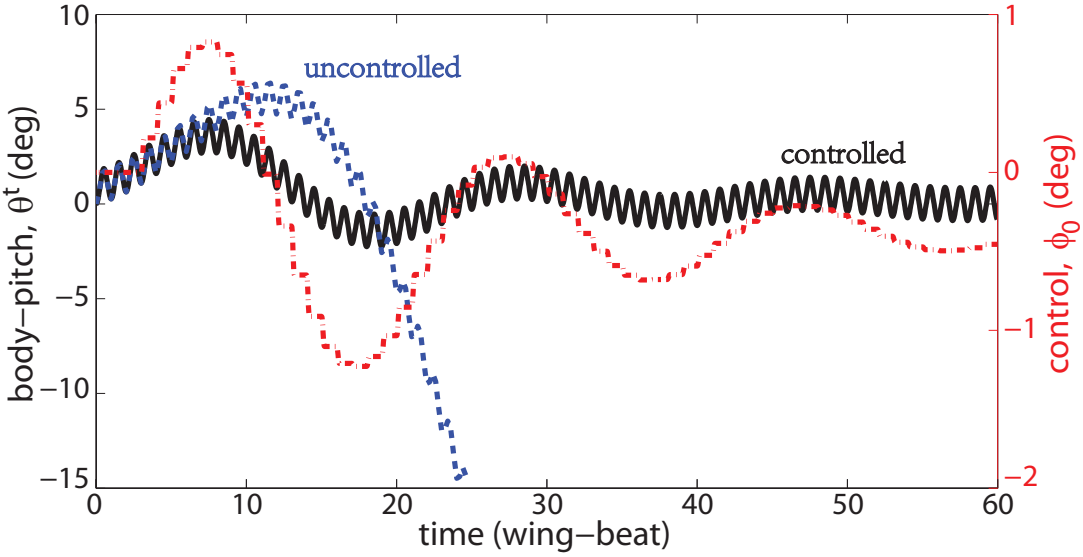

Figure 3.4: Controlled θ^b and the corresponding wing adjustment, ϕ_0. Uncontrolled θ^b is plotted for comparison. The controller parameters are $T_s = 1$ and $T_d = 2$. Note that wing adjustment is minute.

3.4 Constraints on the Sampling Interval and Sensory Delay

With these simulations, we can now answer how fast and how frequently the controller should act in order to stabilize flapping flight. Figure 3.5 shows the effectiveness of the controller in the parametric space spanned by the sampling interval, T_s, and the total delay, T_d, with $T_{d,2} = 0.2$ fixed. For each combination of T_s and T_d, we simulate a controlled free flight for 500 wing-beats. In these simulations, $T_s \geq T_{d,2}$ so that successive control commands do not overlap. We also constrain $|\phi_0| \leq (90^\circ - \phi_m)$ so that the wing stroke amplitude does not exceed 90°. Color indicates the effectiveness of control, which is quantified by the standard deviation of body-pitch, $\Delta\theta$. $\Delta\theta$ is proportional to the oscillation amplitude. For well-controlled flight, $\Delta\theta$ is a few degrees (blue region).

The phase diagram reveals two key results. First, for each sampling interval (T_s), there is a critical sensory delay time (T_{cd}), below which the flight can be controlled. The boundary between the region of well-controlled and poorly-controlled flight is surprisingly sharp and can be approximated by a linear relation, $T_{cd} = 3.2 - 0.5T_s$, as shown by the dashed line in Figure 3.5. For $T_s = 1$ fixed, Figure 3.6(a) shows a transition from a stable flight at $T_d = 2.8$, to an unstable flight at $T_d = 2.9$, and to a more unstable flight at $T_d = 3.2$. At $T_d = 3.2$, the insect tumbles and falls in a similar way as seen in the open-loop simulation.

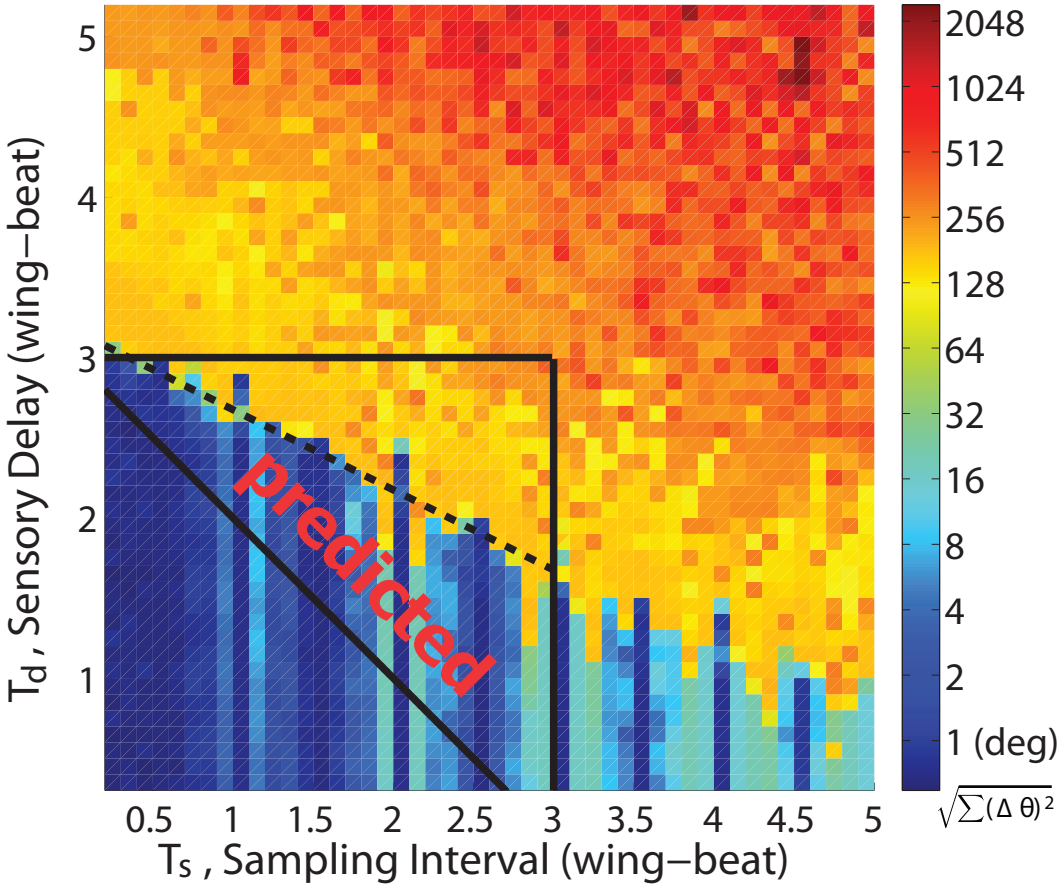

Figure 3.5: The controllability phase diagram. Color represents the sway of body-pitch (in base-2 logarithm scale) in controlled flight measured by the standard deviation of body oscillation in degrees, $\sqrt{\sum(\Delta\theta)^2}$. The solid lines correspond to constraints imposed by the reaction time of fruit flies (Figure3.7). The dashed line is a linear fitting of the critical delay.

Another interesting feature of the phase diagram is that the most effective control occurs at sampling intervals that are integer multiples of a wing-beat, i.e. $T_s = 1, 2, 3, 4, 5$ wing-beats. This is especially pronounced when $T_s > 2$, as indicated by the isolated dark blue bars. As an example, for $T_d = 1.2$ fixed, a small variation near $T_s = 2$ leads to qualitative differences in control performance (Figure 3.6(b)). This sensitivity to the discrete value of T_s reflects the underlying wing flapping time scale. Since the aerodynamic force and torque have a fast oscillation with the wing-beat frequency, θ^b also oscillates with this fast frequency on top of a slower variation given by the body modes. If the kinematics state is measured at a frequency which is a multiple of the wing-beat frequency, the sensed kinematics are taken at the same phase during the wing-beat. This eliminates the fluctuations of θ^b due to variations within a wing-beat and allows the sensor to measure the change of θ^b over a longer time scale, which is the variation that needs to be controlled. In general, sampling at a fractional number of wing-beats leads to overcompensation. In our simulation, one exception is when the sampling time is a multiple of half a wing-beat (e.g $T_s = 1.5, 2.5, 3.5, 4.5$). This is because the induced oscillation of θ^b starts from the neutral position, and its variation is mostly eliminated in half a wing-beat, similar to the case where the sampling interval is an integer number of wing-beats.

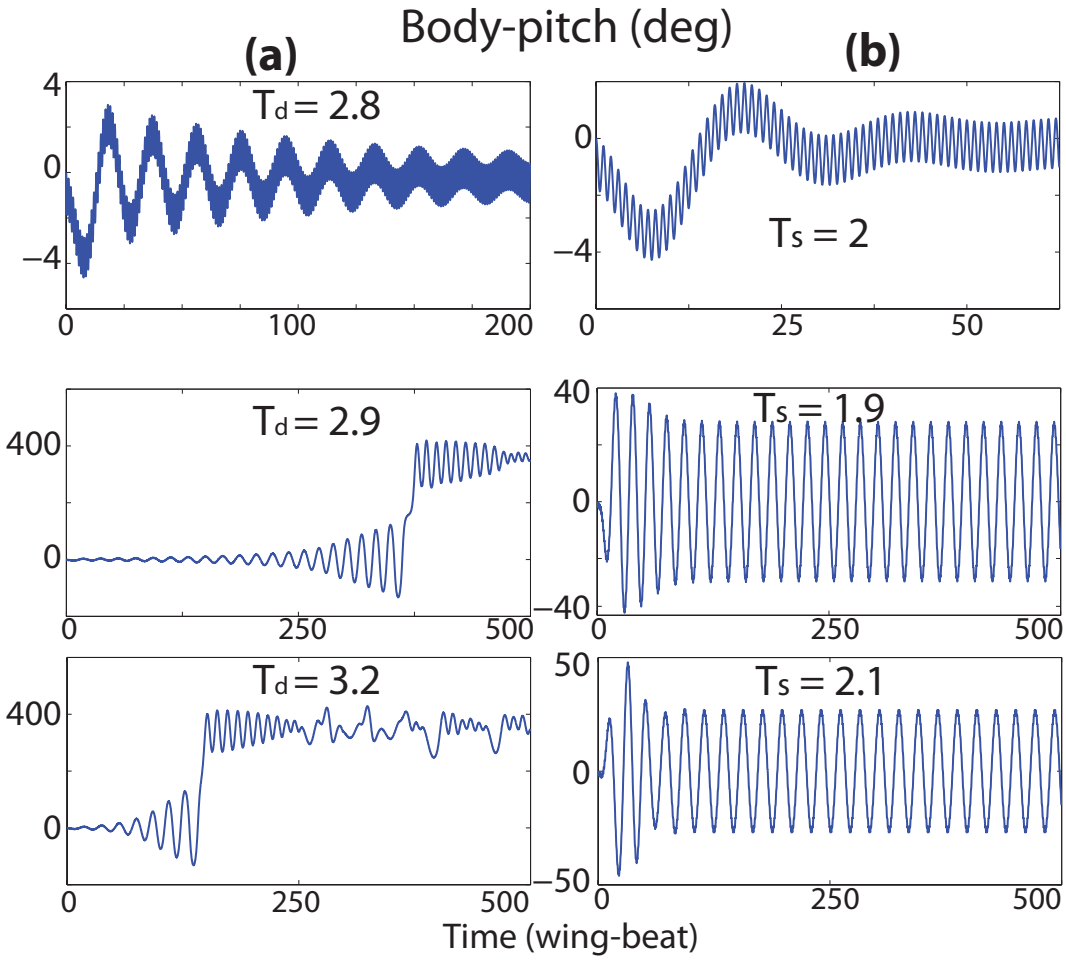

Figure 3.6: θ^b under different control parameters. (a) Varying T_d near the boundary for critical sensory delay, while fixing $T_s = 1$. (b) Varying T_s near $T_s = 2$, while fixing $T_d = 1.2$.

3.5 A Candidate for Beat-to-beat Control in Fruit Flies

Our simulation demonstrates that, using a discrete-sampling, time-delayed, linear controller, it is possible to stabilize flapping flight in the nonlinear regime. We note that the wing adjustment for stabilization is small, which can be easily overlooked by direct observation of flight. The parameter space for controller performance consists of the sampling interval and the sensory delay. The blue region in Figure3.5 suggests a set of parameters that can be used to control a robotic flier.

If our proposed controller is a good approximation of the control strategy employed by fruit flies, we can go one step further to infer that fruit flies sense their body kinematics every wing-beat. Our reasoning is based on the phase diagram (3.5), together with measurements of fruit flies' reaction time [5, 13]. When facing a pulse of torque perturbation, fruit flies respond by adjusting their wing strokes with a delay of about 3 wing-beats. This imposes additional constraints in the parameter space, marked as "predicted" in Figure 3.5. Two of the three solid lines are deduced based on Figure 3.7. First, suppose the torque perturbation occurs shortly after the sensing. The observed 3 wing-beat delay would imply that $T_d + T_s > 3$, which gives the inclined solid line in Figure 3.5. On the other hand, suppose the perturbation occurs just before the sensing. The observed 3 wing-beat delay would imply $T_{d,1} < 3$, which gives the solid line on the top-most boundary. The right-most boundary at $T = 3$ corresponds to a limit beyond which the controller is less robust and only works at an integer number of wing-beats. This leaves two integer choices for the sampling interval, $T_s = 1$ and $T_s = 2$. If we further examine the controller performance in their vicinity, we note that the controller is most robust around $T_s = 1$. At $T_s = 2$, a slight deviation can lead to unstable flight (Figure 3.6(b)). All together, they lead us to conjecture that fruit flies sense their kinematic states every wing-beat.

It remains to be tested whether fruit flier are able to sense their body kinematics every wing-beat to stabilize their flight. Suppose this is true. Such a beat-to-beat controller requires a fast neural pathway. One candidate for this is the neural circuitry between halteres and the first basalar (b1) muscle in flies [47–49]. Halteres are wing-like appendages that beat at wing frequency and act as gyroscopic sensors of body rotation by measuring the Coriolis force [4]. They provide fast inputs to the motor neuron of the b1 muscle via a mono-synaptic electrical pathway, as shown in the studies of blowflies [48]. Unique among all steering muscles, the b1 muscle is the only one that fires a single action potential nearly every wing-beat even during steady flight, whereas other muscles are only active during turning maneuvers [48, 50]. In light of our current results, we suggest that the b1 muscle functions as a flight stabilizer by receiving sensory inputs from the halteres and making small adjustment to the wing motion at a sampling interval of one wing-beat .

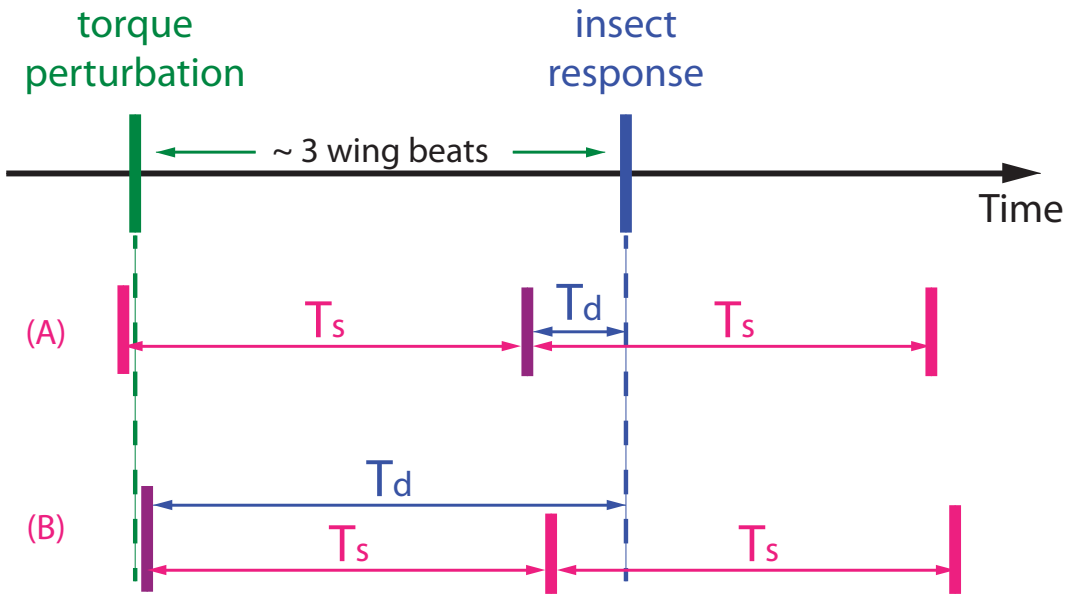

Figure 3.7: Implication of a three-wing-beat reaction time [5] on the relationship between T_s and T_d. We consider two scenarios. The perturbation occurs just after (A) or just before (B) the sensing. In (A), $T_s + T_d \geq 3$. In (B), $T_d \leq 3$. These give two solid lines in Figure 3.5.

3.6 Conclusion

Our simulation of a free flight in open-loop condition revealed the nature of the instability in flapping flight. The insect eventual tumbled and descended, which was a typical motion seen in uncontrolled flapping flight. By tuning model parameters, such as the wing attachment point, and tuning the initial conditions, we tried to locate a hovering flight that is passively stable. Our simulation, however, only found unstable flight whose behavior was similar to the one we showed. This instability resulted from the dynamic coupling between the forward motion of the body-pitch rotation.

We designed a discrete-sampling, time-delayed, linear controller to stabilize flapping flight, based on the sensed body-pitch and body-pitching rate. We used a control strategy that was observed in fruit flies. When designing the controller, we considered two features in neural feedback control: the discrete sampling, and the delayed actuation. The sampling interval and the delay time reflected the fundamental neurophysiological constraints of fruit flies.

We studied how different combinations of the sampling interval and the delay time affected the performance of the body-pitch controller. In the phase diagram representing the controller performance with different combinations of the two time scales, we found two interesting features. First, for each sampling interval, flight was well controlled when the delay time was below a critical value, and the transition from a well controlled flight to a poorly controlled flight was very sharp due to the variation in the delay time. Second, most well controll flight occurred when the sampling interval was an integer number of wing-beats.

Combining our results with experimental findings of the response time of fruit flies to external stimuli, we provided a sharper bound on the sampling interval and the delay

time in the phase diagram. Based on the robustness of the controller, we conjectured that fruit flies relied on a sampling interval around one wing-beat and took control actions with a delay time around two wing-beats. Based on our knowledge of the steering muscles and the sensory organs of fruit flies, we discussed the plausibility of such a beat-to-beat control.

CHAPTER 4

Wing Attachment and Passive Stability of Flapping Flight

Flapping flight may be stabilized by active control schemes as we discussed in the previous chapter. Alternatively, flapping flight of robots and fruit flies may become passively stable by design. Insect-scaled robotic fliers and larger scale ornithopters cannot fly stably without active control, but passive stability can be achieved in their flight by attaching dampers, or damping sails, above their center of mass [1, 27, 51, 52]. On the other hand, fruit flies rely on the halteres and neural feedback control to stabilize their flight. Once the halteres are disabled, fruit flies cannot fly stably, but their flight stability can be restored by attaching dandelion seed fibers dorsally onto their abdomen [5].

Dampers make flight become passively stable, and this can be understood in an aerodynamic analysis. When body undergoes a rotation, aerodynamic drag applies on the dampers, which generates a counter torque that dissipates the body rotation. To a leading order accuracy, this counter torque is proportional to the body rotational velocity [5].

A counter torque may also be induced on flapping wings during body rotation, when the wings co-rotate with the body. Such kind of flapping counter torque is measured on robotic arms that perform both the periodic flapping wing motion and the co-rotation in the body frame [53]. The flapping counter torque opposes the body rotation and is also proportional to the body rotational velocity in a leading order analysis [53, 54].

The similarity between the counter torque on the dampers and the flapping counter torque makes us wonder whether flapping flight can be passively stable. In our open-loop simulation, the flapping counter torque did not stabilize the flight, and we concluded that hovering flight was unstable. Because the flapping counter torque is propor-

tional to the distance between the body center of mass and the wing attachment point, we investigate whether we can achieve passively stable hovering by translating the wings upwards away from the body center of mass.

To answer this question, we first implement our second model of flapping flight, the time-averaged model, from which we may draw conclusions that do not depend on model parameters. This model is similar to models in previous research, where flight dynamics depend on aerodynamic forces and torques that are averaged in time [2, 3, 28].

In our time-averaged model, flapping counter forces are generated by the coupling between the wing motion and body translation, and a flapping counter torque is generated by the coupling between the wing motion and body rotation. We can examine the dynamic effect of the second coupling, or the flapping counter torque. Without the flapping counter torque, we conclude that hovering flight is intrinsically unstable, regardless of where the wings are attached to the body. When the flapping counter torque is considered, the stability of flight depends on the distance between the body center of mass and the wing attachment point. Using parameters for fruit flies, we demonstrate that hovering flight can be achieved by attaching the wings above a certain height over the body center of mass.

Switching back to our 3D dynamic flight model, we study how the elevation of the wing attachment point may affect the stability of flight. We first describe how we find periodic flights in the 3D model and then quantify the linear stability of associated Poinaré maps. The eigenvalues computed from a linearized Poincaré map provide a quantification of the stability of flight.

We find two effects associated with the elevation of the wing attachment point. The first effect is favorable to the flight stability. Once the wing attachment point is above a

critical height, flapping flight becomes passively stable, which qualitatively agrees with what we find in the time-averaged model. The second effect is unfavorable to the vertical lift. Elevating the wing attachment point causes the insect body to oscillate with larger amplitude and results in a smaller vertical lift on average and a descending motion of the model insect. The second effect is not captured by the time-averaged model, which is why the instantaneous wing-body coupling is important. Design of flying robots may choose an optimal wing attachment point to balance between the two effects.

4.1 Analysis in a Time-Averaged Model

4.1.1 Model Insect and Wing Motion

For the subsequent analysis, we simplify the wing motion of the model insect. The wing motion is parallel to a 2D plane spanned by the body longitudinal axis, ζ, and the dorsal-ventral axis, ξ. The wing motion has constant velocity and constant angle of attack during mid-stroke and instantaneous wing reversal at the end of each half stroke. Although this wing motion is different from that seen in fruit flies, with proper choice of wing motion parameters, the time-averaged model generates body modes that are comparable to those from the 3D dynamic flight model, as seen in a later section. We neglect the aerodynamic effect of the wing reversal. Figure 4.1 displays a generic body orientation and the stroke plane. The stroke plane is perpendicular to the body longitudinal axis and co-rotates with the body-pitching motion. The body velocities, u and v, couple with the wing motion and change the effective wing velocity and angle of attack. The effect of the coupling is different in the forward and the backward strokes, both of which are drew in the figure.

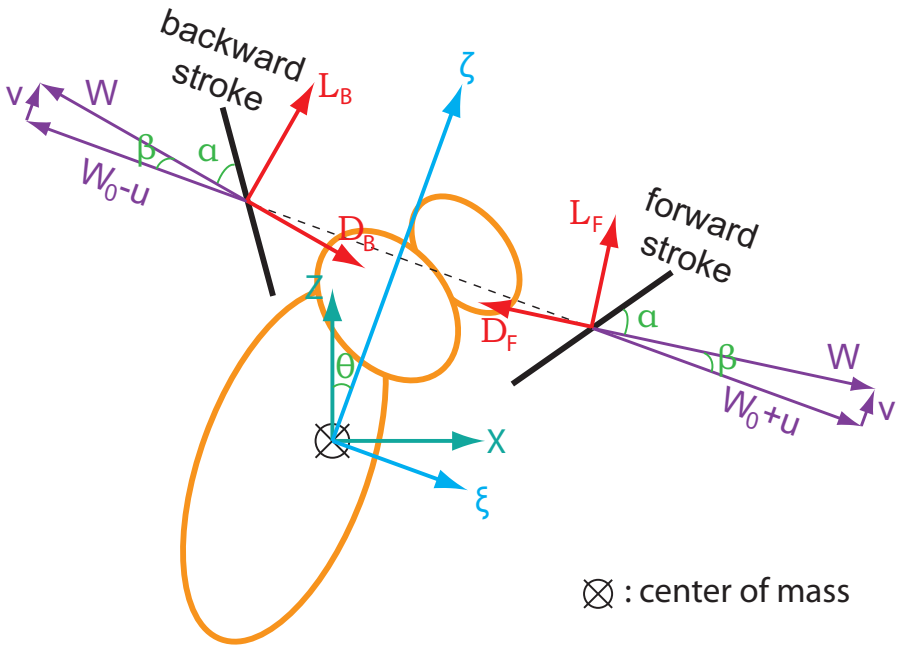

Figure 4.1: Schematic of a model insect in longitudinal flight. The stroke plane is perpendicular to the body longitudinal axis, ζ, and co-rotates with the insect body. Wings in both the forward and backward strokes are drew. In mid-stroke, the wings have constant velocity, W_0, and angle of attack, α_0, relative to the insect body. In the diagram, $\alpha_0 = \alpha + \beta$. The absolute wing velocity, W, and angle of attack, α, are modulated by the body kinematics. The lift, L, is orthogonal to W, and the drag, D, opposes W.

The aerodynamic force follows classic airfoil theory. Two components of the aerodynamic force are considered, a lift, L, and a drag, D. Each component is proportional to the wing area, squared wing velocity, the mass density of the air, and a force coefficient that is a function of the angle of attack,

$$L = \frac{1}{2} c_L(\alpha) \rho_f \bar{c} R W^2 \tag{4.1}$$

$$D = \frac{1}{2} c_D(\alpha) \rho_f \bar{c} R W^2 , \tag{4.2}$$

where ρ_f is the mass density of the air, $\bar{c}$ is the average wing chord, R is the wing span, $\bar{c}R$ gives the wing area, W is the wing translational velocity, and $c_L(\alpha)$ and $c_D(\alpha)$ are the force coefficients. We adopt a parameterization for both force coefficients [55],

$$c_L(\alpha) = C_L \sin 2\alpha \tag{4.3}$$

$$c_D(\alpha) = C_D(1 - \cos 2\alpha) , \tag{4.4}$$

where C_L and C_D are constant pre-factors. This parameterization enables us to express the forces in terms of the components of the wing velocity in the parallel and the perpendicular directions to the wing chord,

$$L = 2 C_L \rho_f \bar{c} R W_{\parallel} W_{\perp} \tag{4.5}$$

$$D = 2 C_D \rho_f \bar{c} R (W_{\perp})^2 , \tag{4.6}$$

where $W_{\parallel}$ is W projected onto the direction parallel to the wing chord, and $W_{\perp}$ is W projected onto the direction perpendicular to the wing chord.

In the following sections, we consider the coupling between the wing motion and body motion. We first consider the coupling between the wing motion and the body translation, which leads to a nonlinear model of flapping flight. We then perform a perturbation analysis and obtain a linear model of the flight dynamics perturbed from hovering. In the linear model, we also consider a second coupling between the wing mo-

tion and the body rotation. In our modeling, the second coupling may only be calculated analytically to the first order of accuracy.

4.1.2 Coupling between the Wing Motion and the Body Translation

Aerodynamic Forces

With respect to the insect body, the wing velocity is W_0, and the angle of attack is α_0 during mid-stroke. The absolute wing velocity and the associated angle of attack are modulated by the body motion. In this section, we first consider the modulation by the body translation. The effect of body rotation is calculated in the next section.

We derive the absolute wing velocity, W, and the angle of attack, α, based on their relative values and the components of the body translational velocity, u and v, which are decomposed in the body frame. u is along the dorsal-ventral axis, and v is along the longitudinal axis. To normalize a frequently encountered prefactor, we resort to the following formula,

$$C_L \rho_f \bar{c} R = \frac{mg}{W_0^2 \sin 2\alpha_0}, \tag{4.7}$$

which is implied by a force balance condition for hovering,

$$mg = C_L \sin 2\alpha_0 \rho_f \bar{c} R W_0^2 . \tag{4.8}$$

The magnitude of the absolute velocity is

$$|W| = |\mathbf{W}_0 + \mathbf{u} + \mathbf{v}| = \sqrt{(W_0 \pm u)^2 + v^2}, \tag{4.9}$$

where $+/-$ is for the forward/backward stroke. In the forward stroke, the parallel and perpendicular components of the wing velocity are, respectively,

$$W_{\parallel,F} = (W_0 + u)\cos\alpha_0 + v\sin\alpha_0 \quad (4.10)$$

$$W_{\perp,F} = (W_0 + u)\sin\alpha_0 - v\cos\alpha_0\,, \quad (4.11)$$

where "F" denotes the forward stroke. The lift is

$$L_F = \frac{2mg}{W_0^2\sin 2\alpha_0}[(W_0 + u)\cos\alpha_0 + v\sin\alpha_0][(W_0 + u)\sin\alpha_0 - v\cos\alpha_0]\,, \quad (4.12)$$

where we drop the $\frac{1}{2}$ factor because there are two wings. In the backward stroke, the velocity components are

$$W_{\parallel,B} = (W_0 - u)\cos\alpha_0 + v\sin\alpha_0 \quad (4.13)$$

$$W_{\perp,B} = (W_0 - u)\sin\alpha_0 - v\cos\alpha_0\,, \quad (4.14)$$

where "B" denotes the backward stroke, and the lift is

$$L_B = \frac{2mg}{W_0^2\sin 2\alpha_0}[(W_0 - u)\cos\alpha_0 + v\sin\alpha_0][(W_0 - u)\sin\alpha_0 - v\cos\alpha_0]\,. \quad (4.15)$$

The calculation for the drag is simila, and we only list the results.

$$D_F = \frac{C_D}{C_L}\frac{2mg}{W_0^2\sin 2\alpha_0}[(W_0 + u)\sin\alpha_0 - v\cos\alpha_0]^2 \quad (4.16)$$

$$D_B = \frac{C_D}{C_L}\frac{2mg}{W_0^2\sin 2\alpha_0}[(W_0 - u)\sin\alpha_0 - v\cos\alpha_0]^2\,, \quad (4.17)$$

where "F" denotes the forward stroke, and "B" denotes the backward stroke.

Nonlinear Time-averaged Model of Flapping Flight

We approximate the total aerodynamic force applied on the insect by the time average of the aerodynamic forces on the wings. Constant wing velocity and angle of attack during

mid-stroke generate constant wing forces during each of the forward and the backward strokes. Because the forward and the backward strokes are symmetric, a time average is reduced to an arithmetic mean of the aerodynamic forces in the two half strokes.

We decompose the total aerodynamic force in the body frame along the ξ and ζ axes,

$$F_\xi = \frac{1}{2}\sin\beta(L_B - L_F) + \frac{1}{2}\cos\beta(D_B - D_F) \quad (4.18)$$

$$F_\zeta = \frac{1}{2}\cos\beta(L_F + L_B) - \frac{1}{2}\sin\beta(D_F + D_B)\,, \quad (4.19)$$

where we have applied $\cot 2\alpha = \frac{1}{2}(\cot\alpha_0 - \tan\alpha_0)$.

The flight dynamics are given by the Newton-Euler equations,

$$\dot{u} = -\omega v + F_\xi/m + g\sin\theta \quad (4.20)$$

$$\dot{v} = \omega u + F_\zeta/m - g\cos\theta \quad (4.21)$$

$$\dot{\theta} = \omega \quad (4.22)$$

$$\dot{\omega} = hF_\zeta/I_y\,, \quad (4.23)$$

where h is the vertical distance from the body center of mass to the wing attachment point and I_y is the body-pitch moment of inertia. The cross terms in the first two equations are due to the decomposition of the translational velocity in the rotating frame.

Simulation

We simulate free flight in the above model and compare the results with those from the 3D dynamic flight model. To match the parameters in the two model, we use the same body mass, moment of inertia along the body-pitch axis, wing-pitch angle during mid-stroke, wing attachment point relative to the body center of mass, and the lift and drag pre-factors. Those parameters are listed in Table 4.1.2. We compute an average

wing velocity, based on the wing-beat frequency and the wing stroke amplitude in the 3D dynamic flight model,

$$W_0 = \frac{8}{3} f R \phi_m \,. \tag{4.24}$$

physical quantity	**symbol**	**value**
body shape	(a^b, b^b, c^b)	$1.2 \times 1.2 \times 2.4$ mm
wing geometry	(a^w, b^w, c^w)	$2 \times 1 \times 10^{-3}$ mm
body mass	m^b	1.1 mg
wing mass	m^w	0.0036 mg
wing beat frequency	f	250 Hz
stroke amplitude (hovering)	ϕ_m	63.13 DEG
deviation from stroke plane	θ_m	0
angle of attack (mid stroke)	ψ_m	38 DEG

Table 4.1: Parameter values used in the time averaged model

In the time-averaged model, an insect starting at stationary and upright remains hovering, because $u = v = \theta = \omega = 0$ is a fixed point of the system. We start our simulation of free flight from a perturbed initial hovering state: $u = v = \omega = 0$, $\theta = 0.01$ rad $\simeq 0.5$ deg. In this case, the body attitude deviates from the upright by 0.01 rad, or approximately 0.5 deg, at the beginning of the simulation. During the simulation, the flight gradually deviates from the hovering equilibrium and enters a tumbling and descending motion, qualitatively similar to the flight behavior as simulated in the 3D dynamic flight model (Figure 4.2). This is the same instability due to the coupling between the forward motion and body-pitch motion.

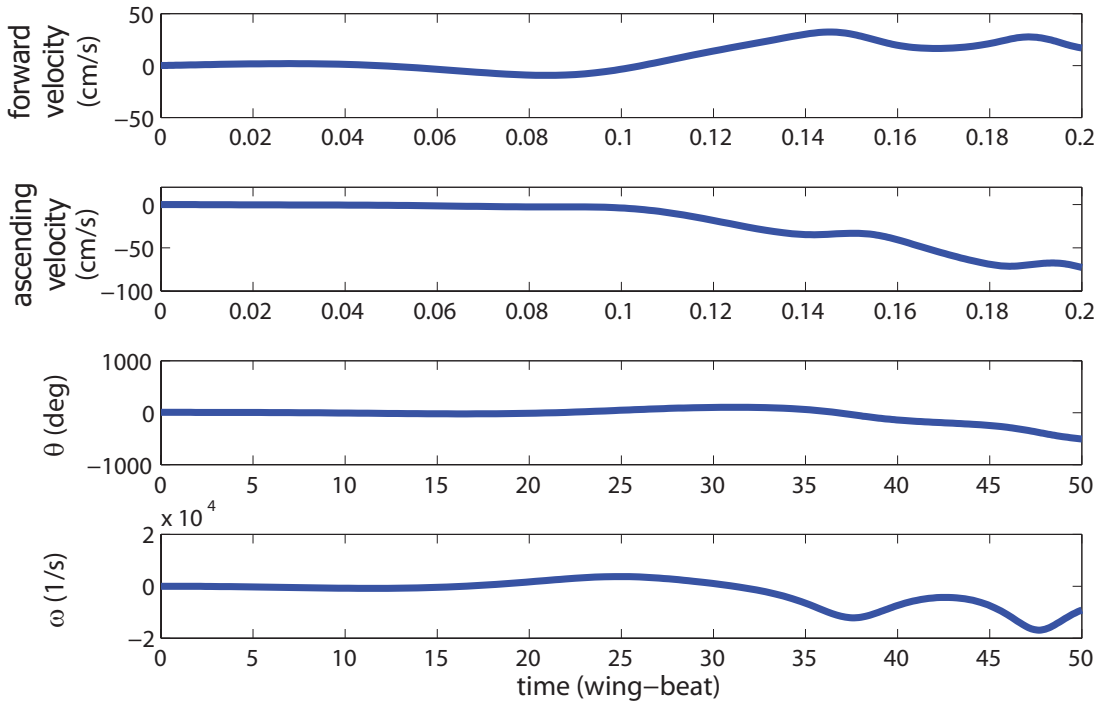

Figure 4.2: Simulation of free flight in the time-averaged model. The insect starts from a stationary initial condition. The initial body attitude is perturbed from the upright orientation by 0.1 rad, roughly 0.5 degree. The flight is unstable in body-pitch, θ and becomes a descending motion.

Perturbation Analysis for Hovering Flight and Linearized Model

We consider body kinematics perturbed from an underlying hovering flight $u_0 = v_0 = \theta_0 = \omega_0 = 0$. The perturbed kinematic variables are $\delta u = u - u_0$, $\delta v = v - v_0$, $\delta\theta = \theta - \theta_0$, $\delta\omega = \omega - \omega_0$. To derived the perturbed dynamics, we compute the aerodynamic forces in our time-averaged model to the leading order in the perturbed kinematics. The perturbed dynamics are thus given by a linear ordinary differential equation system. In the following derivations, we use = sign for precise calculations and $\simeq$ sign for calculations that involve linear expansions.

The wing velocity magnitude is

$$|W| \simeq W_0 \sqrt{1 \pm \frac{2\delta u}{W_0}} \simeq W_0 \pm \delta u\,, \tag{4.25}$$

and the force components are

$$\begin{aligned}
L_F &\simeq mg[1 + \frac{2\delta u}{W_0} + \frac{\delta v}{W_0}(\tan\alpha_0 - \cot\alpha_0)] && (4.26)\\
L_B &\simeq mg[1 - \frac{2\delta u}{W_0} + \frac{\delta v}{W_0}(\tan\alpha_0 - \cot\alpha_0)] && (4.27)\\
D_F &\simeq \frac{C_D}{C_L} mg \tan\alpha_0 (1 + \frac{2\delta u}{W_0} - \frac{2\delta v}{W_0}\cot\alpha_0) && (4.28)\\
D_B &\simeq \frac{C_D}{C_L} mg \tan\alpha_0 (1 - \frac{2\delta u}{W_0} - \frac{2\delta v}{W_0}\cot\alpha_0)\,. && (4.29)
\end{aligned}$$

The deflection of the angle of attack, β, is small in the perturbation analysis, and we apply the following approximations,

$$\begin{aligned}
\sin\beta &\simeq \beta \simeq \tan\beta = \frac{\delta v}{W_0} && (4.30)\\
\cos\beta &\simeq 1\,. && (4.31)
\end{aligned}$$

This leads us to the total forces,

$$\begin{aligned}
F_\xi &\simeq -\left(\frac{C_D}{C_L}\frac{2mg}{W_0}\tan\alpha_0\right)\delta u && (4.32)\\
F_\zeta &\simeq mg - \frac{mg}{W_0}\left(2\cot 2\alpha_0 + \frac{C_D}{C_L}\tan\alpha_0\right)\delta v\,. && (4.33)
\end{aligned}$$

Altogether, the linear dynamical system for the perturbed kinematics are

$$\delta\dot{u} \simeq -\left(\frac{C_D}{C_L}\frac{2g}{W_0}\tan\alpha\right)\delta u + g\theta \tag{4.34}$$

$$\delta\dot{v} \simeq -\frac{g}{W_0}\left(2\cot 2\alpha_0 + \frac{C_D}{C_L}\tan\alpha_0\right)\delta v \tag{4.35}$$

$$\delta\dot{\theta} = \delta\omega \tag{4.36}$$

$$\delta\dot{\omega} \simeq -\frac{mh}{I_y}\left(\frac{C_D}{C_L}\frac{2g}{W_0}\tan\alpha_0\right)\delta u\,. \tag{4.37}$$

4.1.3 Coupling between the Body Rotation and the Wing Flapping Motion

In this section, we calculate the effect of a second coupling between the wing motion and the body rotation. This coupling depends on both the body-pitching rate and the instantaneous position of the wings. As a result, we only calculate the first order effect, a rotational counter torque proportional to the body-pitching rate, and add it to the linear dynamical system in the last section.

In a perturbation analysis, effects due to perturbations in different kinematic variables can be treated separately and then superposed. We thus ignore the body translation in the following analysis. The counter torque does not depend on the body attitude, and thus we simply take $\theta = 0$.

With the perturbed body-pitching rate, $\delta\omega$, the wing velocity becomes dependent on the wing position within the wing stroke,

$$\mathbf{W} = \pm\mathbf{W}_0 + \delta\omega \times (\mathbf{h} + \mathbf{x})\,, \tag{4.38}$$

where $\mathbf{x}$ denotes the wing position along the stroke plane. $x = |\mathbf{x}| \in [-x_0, x_0]$ is the displacement from the center position of the wing stroke, where x_0 is the maximal dis-

placement in relation to the wing stroke amplitude and the wing span. The $+/-$ is for the forward/backward stroke. The aerodynamic forces are,

$$\begin{aligned} \mathbf{L} &= \mp c_L(\alpha)\rho_f A|W|\hat{y} \times \mathbf{W} \\ \mathbf{D} &= -c_D(\alpha)\rho_f A|W|\mathbf{W}\,. \end{aligned}$$

In subsequent analysis, we drop the α variable from the force coefficients. The velocity has the magnitude

$$\begin{aligned} |W| &= |\pm \mathbf{W}_0 + \delta\omega \times (\mathbf{h} + \mathbf{x})| \\ &\simeq \sqrt{W_0^2 \pm 2\mathbf{W_0} \cdot \delta\omega \times (\mathbf{h} + \mathbf{x})} \\ &= \sqrt{W_0^2 \pm 2W_0\hat{\xi} \cdot \delta\omega\hat{y} \times (h\hat{\zeta} + x\hat{\xi})} \\ &\simeq W_0 \pm \delta\omega h \end{aligned}$$

where $\hat{\xi}$ and $\hat{\zeta}$ denote the unit vectors along the two body frame axes, and $\hat{y}$ is the unit vector in the body transverse direction pointing into the paper (Figure 4.1). The $\simeq$ sign denotes linear expansions.

We first compute the counter-torque generated by the lift, and we treat the contribution by the forward and backward strokes separately. In the forward stroke,

$$\begin{aligned} \tau_{\mathbf{L,F}} &= -c_L\rho_f A|W|(\mathbf{h} + \mathbf{x}) \times (\hat{y} \times \mathbf{W}) \\ &= -c_L\rho_f A|W|(h\hat{\zeta} + x\hat{xi}) \times [\hat{y} \times (W_0\hat{xi} + \delta\omega\hat{y} \times (h\hat{\zeta} + x\hat{xi}))] \\ &= -c_L\rho_f A|W|(h\hat{\zeta} + x\hat{xi}) \times [-W_0\hat{\zeta} + \delta\omega\hat{y} \times (h\hat{xi} - x\hat{\zeta})] \\ &= -c_L\rho_f A|W|(h\hat{\zeta} + x\hat{xi}) \times [-(W_0 + \delta\omega h)\hat{\zeta} + \delta\omega x\hat{xi}] \\ &= -c_L\rho_f A|W|(W_0 + 2\delta\omega h)x\hat{y} \\ &\simeq -c_L\rho_f A(W_0 + \delta\omega h)(W_0 + 2\delta\omega h)x\hat{y} \\ &\simeq -c_L\rho_f AW_0^2(1 + \frac{3\delta\omega h}{W_0})x\hat{y}\,. \end{aligned}$$

In the backward stroke, the counter torque due to the lift is obtained by reversing the sign of W_0,

$$\begin{aligned}\tau_{\mathbf{L,B}} &\simeq -c_L\rho_f A(-W_0+\delta\omega h)(-W_0+2\delta\omega h)x\hat{y}\\ &\simeq -c_L\rho_f AW_0^2(1-\frac{3\delta\omega h}{W_0})x\hat{y}\,. \end{aligned} \tag{4.39}$$

On average, the contributions from the two half-strokes sum to a linear term in x, $-c_L\rho_f AW_0^2 x\hat{y}$, and

$$\frac{1}{2x_0}\int_{-x_0}^{x_0} -c_L\rho_f AW_0^2 x\hat{y}dx = 0\,. \tag{4.40}$$

Here, the integration is conducted in x by a change of variable. As a result, the counter torque due to the lift is zero in the first order approximation.

Similarly, the counter torque due to the drag is computed, and the results are listed below. In the forward stroke,

$$\begin{aligned}\tau_{\mathbf{D,F}} &= -c_D\rho_f A|W|(\mathbf{h}+\mathbf{x})\times\mathbf{W}\\ &\simeq -c_D\rho_f A(W_0+\delta\omega h)[(h\hat{\zeta}+x\hat{xi})\times((W_0+\delta\omega h)\hat{xi}-\delta\omega x\hat{\zeta}))]\\ &= -c_D\rho_f A(W_0+\delta\omega h)[W_0 h+\delta\omega(h^2+x^2)]\hat{y}\\ &\simeq -\frac{c_D}{c_L}c_L\rho_f AW_0^2 h(1+\frac{2\delta\omega h}{W_0}+\frac{\delta\omega x^2}{hW_0^2})\hat{y}\\ &= -mgh\frac{c_D}{c_L}(1+\frac{2\delta\omega h}{W_0}+\frac{\delta\omega x^2}{hW_0})\hat{y}\,, \end{aligned} \tag{4.41}$$

where, in the last equality, we apply the force balance condition at hovering. In the backward stroke,

$$\begin{aligned}\tau_{\mathbf{D,B}} &\simeq -c_D\rho_f A(W_0-\delta\omega h)[-W_0 h+\delta\omega(h^2+x^2)]\hat{y}\\ &= -mgh\frac{c_D}{c_L}(-1+\frac{2\delta\omega h}{W_0}+\frac{\delta\omega x^2}{hW_0})\hat{y}\,. \end{aligned} \tag{4.42}$$

The contributions from the two half-strokes average out to $-mgh\frac{c_D}{c_L}(\frac{2\delta\omega h}{W_0}+\frac{\delta\omega x^2}{hW_0})$, a constant independent of x plus a quadratic term in x. The time average is

$$\tau_D = \frac{1}{2x_0}\int_{-x_0}^{x_0}\frac{1}{2}(\tau_{D,F}+\tau_{D,B})dx$$

$$= -mg\frac{c_D}{c_L}\frac{2h^2}{W_0}(1+\frac{x_0^2}{6h^2})\delta\omega\,, \tag{4.43}$$

which is proportional to the perturbed body-pitching rate. This term is added to the linear time-averaged model, and the dynamical system becomes

$$\delta\dot{u} \simeq -\left(\frac{C_D}{C_L}\frac{2g}{W_0}\tan\alpha\right)\delta u \tag{4.44}$$

$$\delta\dot{v} \simeq -\frac{g}{W_0}\left(2\cot 2\alpha_0 + \frac{C_D}{C_L}\tan\alpha_0\right)\delta v \tag{4.45}$$

$$\delta\dot{\theta} = \delta\omega \tag{4.46}$$

$$\delta\dot{\omega} \simeq -\frac{h}{I_y}\left(\frac{C_D}{C_L}\frac{2mg}{W_0}\tan\alpha_0\right)\delta u - \frac{h^2}{I_y}\left(\frac{c_D(\alpha)}{c_L(\alpha)}\frac{mg}{W_0}(1+\frac{x_0^2}{6h^2})\right)\delta\omega\,. \tag{4.47}$$

The added term depends on the value of h, or the wing attachment point. In the limit where $h >> x_0$, τ_D increases with h^2 and may stabilize the flight naturally.

4.1.4 Wing Attachment and Passive Flight Stability in Time-averaged Model

The dynamics of the linearized time-averaged model are expressed in a matrix form,

$$\begin{pmatrix}\delta u\\ \delta v\\ \delta\theta\\ \delta\omega\end{pmatrix} = \begin{bmatrix}-a & 0 & g & 0\\ 0 & -c & 0 & 0\\ 0 & 0 & 0 & 1\\ -a\frac{mh}{I_y} & 0 & 0 & -b\end{bmatrix}\begin{pmatrix}\delta u\\ \delta v\\ \delta\theta\\ \delta\omega\end{pmatrix} \tag{4.48}$$

where $a = \left(\frac{C_D}{C_L}\frac{2g}{W_0}\tan\alpha\right)$, $b = \frac{h^2}{I_y}\left(\frac{c_D(\alpha)}{c_L(\alpha)}\frac{mg}{W_0}(1+\frac{x_0^2}{6h^2})\right)$, and $c = \frac{g}{W_0}\left(2\cot 2\alpha_0 + \frac{C_D}{C_L}\tan\alpha_0\right)$. The characteristic equation of this linear ordinary differential equation system is

$$(\lambda + c)\left[\lambda^3 + (a+b)\lambda^2 + ab\lambda + \frac{mgh}{I_y}\right] = 0\,. \tag{4.49}$$

The dynamic stability of hovering flight depends on the roots of this characteristic equation. A first root is found at $\lambda = -c$, which corresponds to a perturbation in the vertical flight. The remaining three roots are solved from the cubic equation,

$$\lambda^3 + (a+b)\lambda^2 + ab\lambda + \frac{mgh}{I_y} = 0\,. \tag{4.50}$$

Among the coefficients, b appears in the linear term in the characteristic equation and increases with h^2 when $h >> x_0$. In a previous derivation of a time-averaged model of longitudinal flapping flight, the linear coefficient in the characteristic equation is related to the damping rate of the body-pitch rotation [5]. Increasing the damping rate may lead to a passively stable flapping flight, which suggests that hovering flight can be passively stable for large h values in our model, i.e. for wing attachment point sufficiently high above the body center of mass.

The cubic equation can be solved analytically only for special values of h. For example, when $h = 0$, i.e. when the wings are attached to the body center of mass, the characteristic equation has roots $\lambda = 0, -a, -b, -c$. The system is neutrally unstable because of the zero eigenvalue. For general values of h, we solve for the roots of the characteristic equation numerically, using typical parameters for fruit flies. For $-6L \leq h \leq 6L$, where L stands for half of the body length, we plot the real parts of the roots of the characteristic equation in Figure 4.3. These are also the eigenvalues of the time-averaged system. For a passively stable hovering, all eigenvalues should have negative real parts.

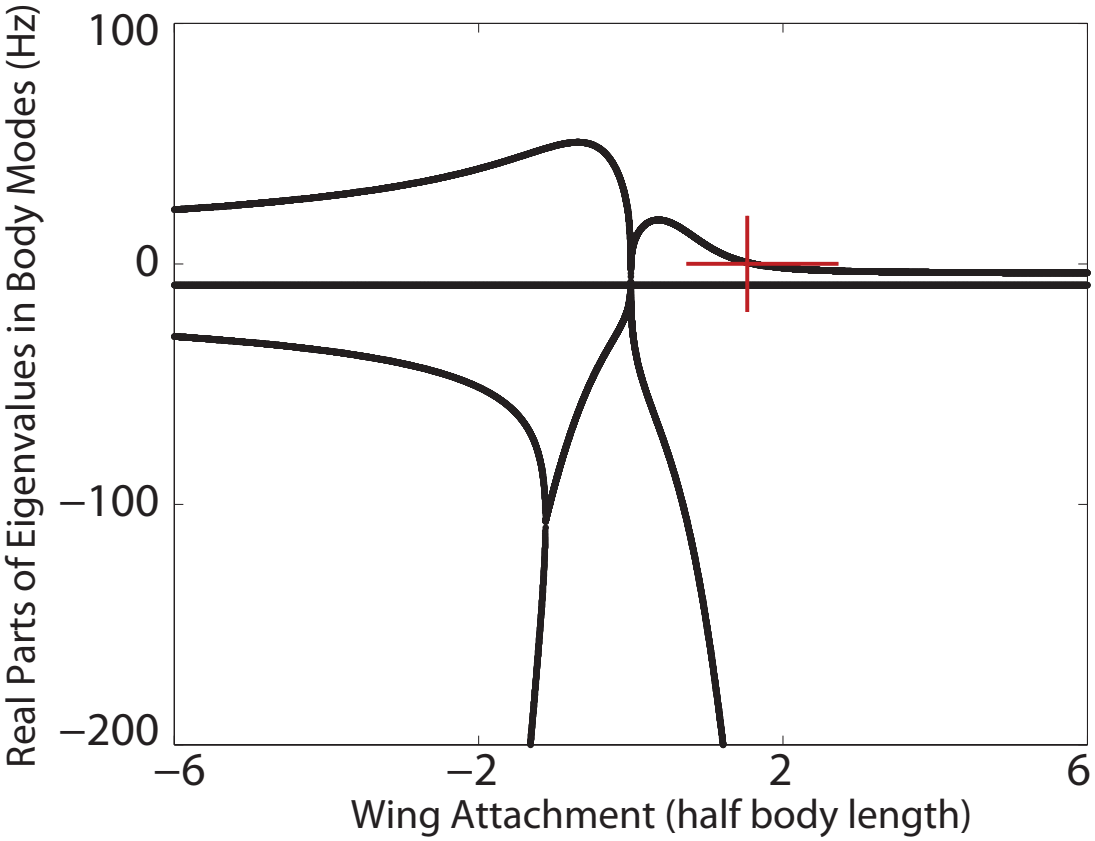

Figure 4.3: Body modes (real parts) for various wing attachment positions. The wing attachment is normalized by the half body length. Red cross-hair denotes the critical wing attachment of 1.53 half body length above the center of mass. This is a critical value above which the time-averaged flight system is passively stable.

As shown in the figure, flapping flight is unstable when wings are below the center of mass ($h < 0$). We can also infer this general conclusion from the characteristic equation, which has a negative constant term due to $h < 0$. Flight is thus unstable, by the stability theorem of Routh-Hurwitz. Flapping flight is neutrally unstable where the wings are at the center of mass ($h = 0$), due to the zero eigenvalue. When $0 < h < 0.36$, flight become more unstable with the increase in h, or the elevation of the wing attachment point. For $0.36 < h < 1.6$, the flight becomes less unstable with the elevation of the wings. At $h = 1.6$, the system reaches another neutrally unstable point due to a zero eigenvalue. This critical h value at 1.6 is marked with a red cross. As h increases above the critical value of 1.6, flight is passively stable. The constant eigenvalue corresponds to the vertical flight mode that is independent of h. The range of h values studied here is wide enough for us to cover the cases studied in experiments [1, 51].

Lastly, in a special case where the counter torque due to the wing motion and the body rotation is neglected, we are able to draw another general conclusion on the dynamic stability of flapping flight. Setting $b = 0$, we rewrite the characteristic equation as

$$(\lambda + c)(\lambda^3 + a\lambda^2 + a\frac{mgh}{I_y}) = 0\,. \tag{4.51}$$

Besides the fixed pole at $\lambda = -c$, the stability of the system depends on the roots of the a cubic equation,

$$\lambda^3 + a\lambda^2 + a\frac{mgh}{I_y} = 0\,. \tag{4.52}$$

The stability theorem of Routh-Hurwitz [56] implies an intrinsic instability of the system, resulting from the missing linear term in the cubic equation.

Alternatively, one can verify by basic algebra that there is at least one eigenvalue whose real part is greater than zero. Here we proceed by assuming that $h > 0$ and show that the system has an unstable complex mode. One can also show that the system has positive real modes when $h < 0$ and the system is neutrally unstable when $h = 0$. The negative determinant, $\Delta = -4a^4\frac{mgh}{I_y} - 27\left(a\frac{mgh}{I_y}\right)^2 < 0$, indicates that the cubic equation has one real root and two complex conjugate roots. Let λ_1 be real, and $\lambda_{2,3} = r \pm jq$, ($j^2 = -1$), where r and q are real. It follows from Viete's Formula that

$$\lambda_1 + \lambda_2 + \lambda_3 = \lambda_1 + 2r = -a < 0 \tag{4.53}$$

$$\lambda_1\lambda_2 + \lambda_2\lambda_3 + \lambda_3\lambda_1 = 2\lambda_1 r + r^2 + q^2 = 0 \tag{4.54}$$

$$\lambda_1\lambda_2\lambda_3 = \lambda_1(r^2 + q^2) = -a\frac{mgh}{I_y} < 0\,. \tag{4.55}$$

These formula imply that $\lambda_1 < 0$ and $r > 0$. The system is always unstable, regardless of the choice of model parameters such as h.

A linear term in the cubic equation may also arise, for example, from an aerodynamic damping on the insect body, besides the effect of wing attachment point that we study here. Because our underlying flight mode is hovering, including a substantial aerodynamic damping on the body may not be appropriate. In fact, except for extreme cases such as the woolly aphid, most flying insects cannot rely on body damping to attain passive flight stability [3, 5].

4.2 Analysis in 3D Dynamic Flight Model

In this section, we study the effect of wing attachment point on the flight stability, using our 3D dynamic flight model. Because the 3D dynamic model is driven by periodic flapping wing motions and time dependent, we cannot rely on the method of linear

stability analysis for equilibrium flights. Instead, we first have to locate the periodic flights in the dynamic model [34, 57], which are the counterparts of the equilibrium flights in the time-averaged model. We then describe the linear stability analysis for Poincaré maps associated with the periodic flights.

4.2.1 Periodic Flight and Linear Stability Analysis of Associated Poincaré Map

We need to identify the periodic solutions in the 3D dynamic flight model before quantifying the stability [34, 57]. The fundamental period of the system is a wing-beat denoted by T. We solve for periodic flights by searching for an initial body kinematic state, x_0, such that

$$\phi(t_0 + qT; t_0, x_0) - x_0 = 0\,, \tag{4.56}$$

where q is a fixed integer, and $\phi(t; t_0, x_0)$ denotes the solution at t, starting from initial state x_0 at initial time t_0. In our computation, we take $t_0 = 0$, when the two wings start beating from the center position of the wing stroke. The body kinematics thus needs to return to the initial state after q wing-beats. This is a two-point boundary value problem with a periodic boundary condition. It is equivalent to a nonlinear root finding problem, which is solved for the unknown x_0. We use the Newton-Raphson method to find the root of this nonlinear equation. The iteration is given by

$$x_{n+1} = x_n + \left(1 - \frac{\partial \phi}{\partial x}\Big|_{x_n}\right)^{-1} [\phi(T; 0, x_n) - x_n]\,, \tag{4.57}$$

where x_n denotes the previous solution, and x_{n+1} is the updated solution. In longitudinal flight, the state variable, x, comprises the translational velocities, u and v, and the body-pitch attitude and rate, θ and ω. In computation, we stop the iteration after the computed series or roots reaches a numeric convergence, $|x_{n+1} - x_n| < \epsilon_r |x_n|$, where ϵ_r is a relative tolerance level. We then take x_{n+1} as an approximated solution to the periodic flight problem, and the solution is within a relative error of ϵ_r from the true solution x_0.

Figure 4.4 shows a periodic flight with a period of one wing-beat. The body translational velocity is close to zero, due to an almost balance of forces and torques on the body. By varying the integer q and changing the initial trial solution, we attempt to seek flights whose periods are multiples of a wing-beat period. We have only obtained period-1 flights in our study.

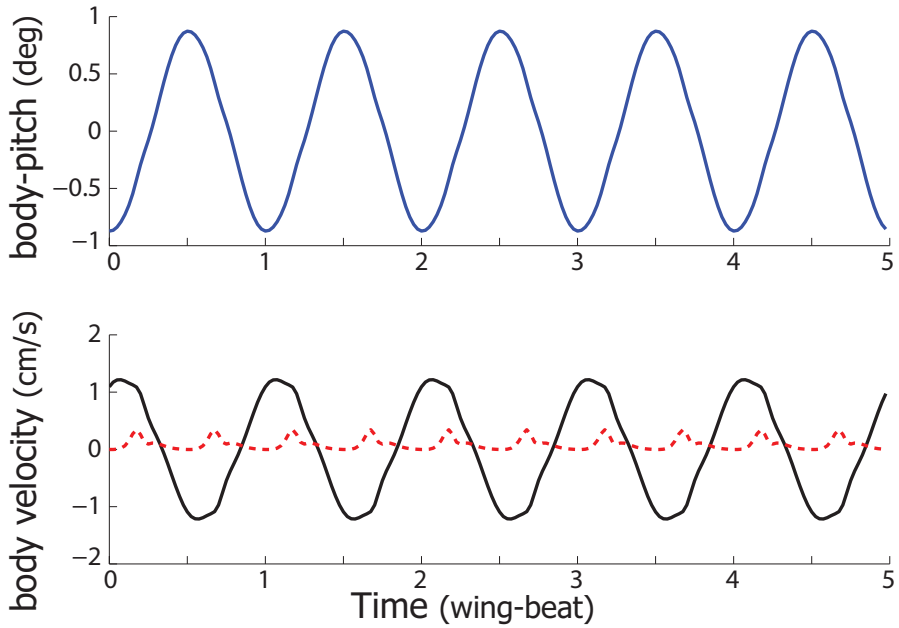

Figure 4.4: Flight trajectory of a periodic equilibrium flight with almost zero velocity. (Blue) body-pitch attitude, (red) ascending velocity, (black) forward velocity. The frequency doubling in v velocity agrees with what is exhibited by the open-loop simulation.

The stability of a periodic flight can be evaluated using linear stability analysis on the associated Poincaré return map. The initial condition, x_0 with $\phi(T; 0, x_0) - x_0 = 0$, depends on the initial phase of the periodic wing motion. In our computation, the wings start flapping from the center position of the wing stroke, and this defines a Poincaré section with which the periodic flight trajectory intersects at x_0 4.5. Let ϵ_0 be a small perturbation to x_0 at time 0. In a linear order approximation, the perturbation ϵ_n at time nT evolves with the following iteration,

$$\epsilon_{n+1} = \left[\frac{\partial \phi}{\partial x}(x_0)\right] \epsilon_n, \tag{4.58}$$

for $n = 0, 1, 2, \ldots$, provided that all perturbations are small so that the linear approximation is warranted. $\left[\frac{\partial \phi}{\partial x}(x_0)\right]$ is a 4×4 matrix. The periodic flight is stable if and only if all eigenvalues of this matrix have modulus less than 1, ($|\Lambda_i| < 1$) for $i = 1, 2, 3, 4$. We let $\lambda_i = \frac{1}{T} \ln \Lambda_i$. For the flight system to be stable, the real parts of all λ_i's need to be negative. The four eigenvectors of this matrix correspond to the characteristic modes of hovering flight.

x_0	1.1 cm/s	9.7×10^{-3} cm/s	-1.5×10^{-2} rad	-0.64 /s
λ_i s^{-1}	$19 + 44j$	$19 - 44j$	-61	-3.2
$\mathbf{e}_i$	(mode A)	(mode A)	(mode B)	(mode C)
δu (cm/s)	$0.24 + 0.28j$	$0.24 - 0.28j$	0.28	4.0×10^{-3}
δv (cm/s)	$(-3.2 - 4.0j) \times 10^{-3}$	$(-3.2 - 4.0j) \times 10^{-3}$	-3.7×10^{-3}	1.0
$\delta\theta$ (rad)	$(-0.8 + 1.7) \times 10^{-2}$	$(-0.8 - 1.7) \times 10^{-2}$	-1.5×10^{-2}	0
$\delta\omega$ (1/s)	-9.3	-9.3	9.6	-1.6×10^{-2}

Table 4.2: Periodic flight, x_0, the eigenvalues, λ_i's, and eigenvectors, $\mathbf{e}_i$'s, ($i = 1, 2, 3, 4$) of the associated 4×4 matrix, $\left[\frac{\partial \phi}{\partial x}(x_0)\right]$. The flight is near hovering.

In our simulation, the located periodic flight is close to a hovering flight because of a small body-pitch oscillation and a weight-balancing lift. The solved initial condition, x_0, together with the eigenvalues and the eigenvectors of the 4×4 matrix are listed in Table 4.2. From the row of λ_i's, we note that the flight has an unstable complex mode

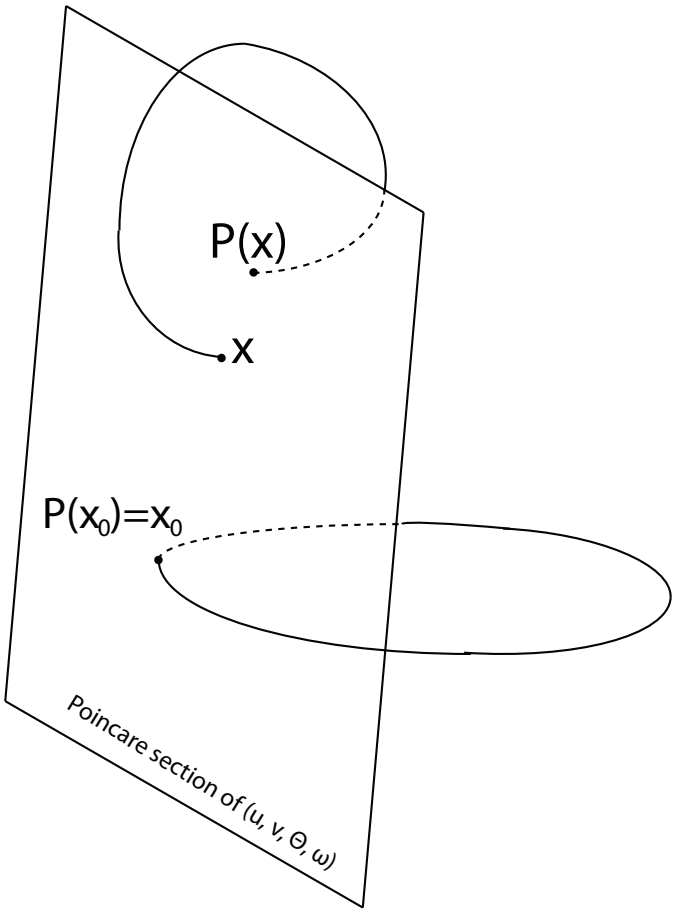

Figure 4.5: Schematic drawing of the Poincaré return map. $\mathcal{P}$ is the return map. x is a generic system state at $t = 0$ from the Poincaré section corresponding to the initial phase of the wing motion. $\mathcal{P}(x)$ is the state at $t = T$ along the solution curve, where T is the wing-beat period. x_0 is a fixed point of the map, because $\mathcal{P}(x_0) = x_0$, and represents a periodic flight. x_0 depends on the location of the Poincaré section, or the initial phase of the wing motion.

and two stable real modes, as predicted by our time-averaged model of hovering flight, which is also the same as what was claimed in previous research ([2, 35]).

The eigenvectors are not normalized. To compare the magnitudes of the components, we choose 1 cm/s for velocity scale and 1 rad for the scale of body attitude. We find a scale for the body-pitching rate from the dynamic equation for body-pitch in our time-

averaged model,

$$\delta\dot{\omega} \simeq -\frac{h}{I_y}\left(\frac{C_D}{C_L}\frac{2mg}{W_0}\tan\alpha_0\right)\delta u - \frac{h^2}{I_y}\left(\frac{c_D(\alpha)}{c_L(\alpha)}\frac{mg}{W_0}(1+\frac{x_0^2}{6h^2})\right)\delta\omega\,. \tag{4.59}$$

We choose a scale of 10 /s for the body-pitching rate such that the two "torques" in the equation contribute almost equally. After the normalization, the components of each eigenvector, $\mathbf{e}_i$, are different by 2 to 3 orders of magnitude. We draw each of the body modes in Figure 4.6, while neglecting the relatively small components. Mode A corresponds to the unstable complex mode, a combination of a nose-up body-pitch rotation and a forward translation. We perform a static stability analysis by analyzing the initial response. The coupling between δu and the wing motion induces a net drag, F_D, on the wings, which points in the dorsal direction. The drag incurs a torque, τ, which points in the same direction as the body rotation. This mode is thus statically unstable. Because static instability implies dynamic instability, mode A is dynamically unstable. Mode B is different from mode A by the direction in which the body rotates. The induced torque now points in the opposite direction of the body rotation, and the mode is stable. Mode C corresponds to the last mode, $\mathbf{e}_4$, a perturbation to the vertical flight. This mode is also stable.

4.2.2 Comparison of Body Modes between the Models

We compare the results of stability analysis from both the time-averaged model and the 3D flight model. For hovering fruit flies, we compare the body modes computed from the two models. We also include several results from earlier research into our comparison. In Table 4.3, we list the body modes from both our models, together with those from other studies. We find that all the studied longitudinal flights are unstable and characterized by the same three modes in Figure 4.6: an unstable oscillatory mode,

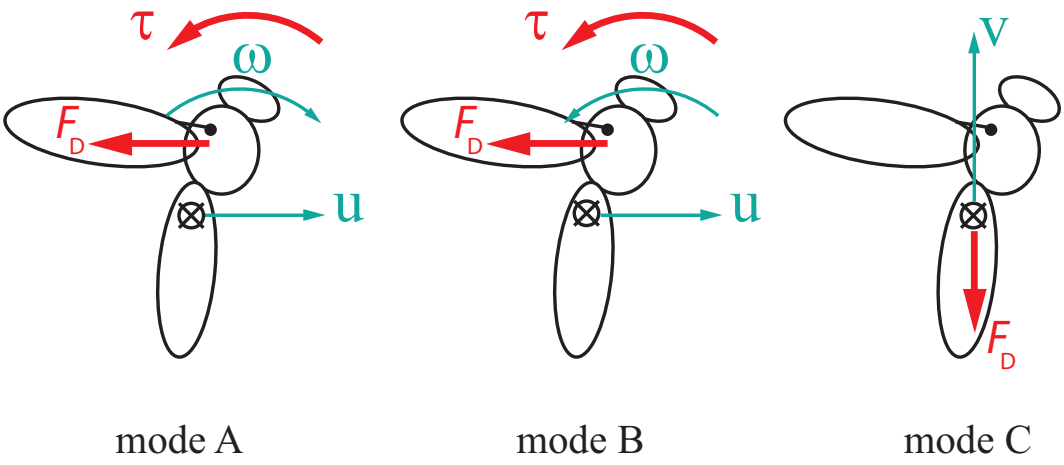

Figure 4.6: Three characteristic modes from the analysis of periodic hovering flight in 3D dynamic flight model. Symbols: u, forward velocity; v, ascending velocity; ω, body-pitch velocity; τ, aerodynamic counter torque; F_D, aerodynamic drag. Mode A is unstable because the torque generated by the coupling of wing motion and body translation points in the same direction as the body-pitch rotation. On the other hand, mode B and mode C are stable, because the torque points in the direction against the body-pitch rotation.

a fast subsidence mode, and a slow subsidence mode (the vertical flight mode). For our time-averaged model, we also compare the results either with or without the counter-torque due to the coupling between the wing motion and the body rotation. We do not see qualitative difference between the two cases, although the eigenvalues computed with the rotational counter torque are closer to the results from the 3D dynamic flight model.

One important assumption for the time-averaged model is that the wing flapping frequency is much greater than the frequencies of body modes, otherwise the force averaging is not warranted. In our simulation, the 3D dynamic flight model and the time-averaged model yield similar results, because the fruit fly's wing-beat frequency is over 200 Hz, roughly 10 times the growth rate of the unstable mode. On the other hand, numerical analysis of the dynamic stability in hawk moths showed a discrepancy

flying insects	simulation method	$\lambda_{1,2}$ [s^{-1}]	λ_3	λ_4
Fruit fly	nonlinear	$19 \pm 44j$	-61	-3.2
Fruit fly	linear†	$27 \pm 50j$	-61	-8.7
Fruit fly	linear‡	$18 \pm 49j$	-70	-8.7
Hoverfly [35]	linear	$12 \pm 23j$	-27	-3.2
Cranefly [3]	linear	$3.3 \pm 6.3j$	-7.5	-0.68
Dronefly [3]	linear	$5.2 \pm 115j$	-136	-17
Hawk moth [3]	linear	$7.1 \pm 16j$	-20	-2.4
BumbleBee [35]	linear	$7.0 \pm 20j$	-31	-1.9
Dronefly [29]	nonlinear	$7.8 \pm 16j$	-19	-2.4
Dronefly [29]	linear	$7.8 \pm 15j$	-19	-2.4
Hawk moth [29]	nonlinear	$5.2 \pm 15j$	-19	-2.7
Hawk moth [29]	linear	$6.6 \pm 15j$	-19	-2.5

Table 4.3: Body modes of flying insects. † Time-averaged model without the rotational counter torque. ‡ Time-averaged model with the rotational counter torque.

between a time-averaged model and a model with the instantaneous coupling [34].

We would like to test the applicability of the time-averaged model. In Table 4.4, we list the computed eigenvalues from both models, when the wing frequency is reduced from 250 Hz to 62.5 Hz. In the computation using the time-averaged model, we include the rotational counter-torque. To maintain the weight balance in both models, we increase the wing area and keep its aspect ratio. In the table, the difference between the models increases with the decrease in the wing-beat frequency. This may indicate that force averaging is not warranted when wing frequency is too low, if the 3D dynamic flight model always generates accurate results. This comparison is also portrayed in Figure 4.7. The red arrows depict directions in which the wing-beat frequency is lowered. When we use the wing-beat frequency of fruit flies' in the models, the dynamic analyses lead us to very close results.

Frequency/Hz	simulation method	$\lambda_{1,2}$	λ_3	λ_4
250	3D Dynamics	$19 \pm 44j$	-61	-3.2
250	time-averaged	$18 \pm 49j$	-71	-8.7
200	3D Dynamics	$16 \pm 39j$	-55	-3.0
200	time-averaged	$18 \pm 51j$	-75	-9.8
160	3D Dynamics	$13 \pm 34j$	-46	-2.0
160	time-averaged	$16 \pm 53j$	-81	-11
125	3D Dynamics	$11 \pm 28j$	-33	-3.8
125	time-averaged	$14 \pm 54j$	-89	-12
100	3D Dynamics	$9.8 \pm 24j$	-31	-3.6
100	time-averaged	$13 \pm 55j$	-97	-14
80	3D Dynamics	$9.2 \pm 20j$	-31	-2.2
80	time-averaged	$10 \pm 56j$	-108	-15
62.5	3D Dynamics	$7.0 \pm 19j$	-27	2.5
62.5	time-averaged	$6.3 \pm 55j$	-127	-18

Table 4.4: Eigenvalues of flapping flight systems with different wing-beat frequencies. The eigenvalues are non-dimensionalized by the wing-beat frequencies.

4.2.3 Wing Attachment and Dynamic Flight Stability

We study how changes in wing attachment point affect the dynamic stability of flight. We use the same length scale, the half body length, to denominate the vertical distance from the wing hinges to the body center of mass. In our previous studies of hovering flight, $h = 0.8$. Here we elevate the wings from $h = 0.8$ to $h = 6$. We solve for periodic flights for different wing attachment points and evaluate the stability of the flights.

Figure 4.8 displays the real parts of the eigenvalues of the linearized Poincaré maps associated with the periodic flights. We compare this figure with the result from the time-averaged model. We note a similar transition from intrinsically unstable flight to passively stable flight as h increases. The critical h value is 2.2 in the current model. One of the body modes, the vertical flight mode, is weakly coupled with h. This is similar to the time-averaged model where the vertical flight mode is independent of h.

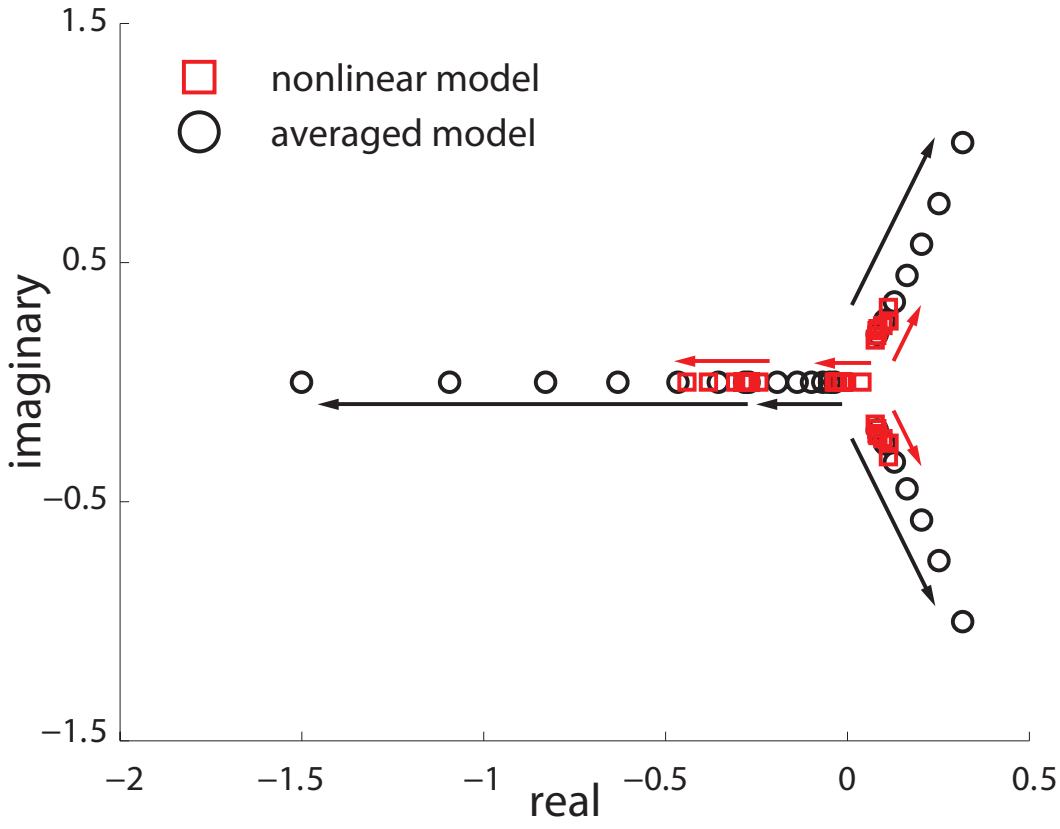

Figure 4.7: Eigenvalues of body modes for different wing-beat frequencies. Results from both the 3D dynamic flight model and the time-averaged model are shown. The arrows points to the direction in which the wing-beat frequency drops.

We also notice differences between the two models. First, the critical height of wing attachment point is $h = 2.2$ in the 3D dynamic flight model, which is different from $h = 1.6$ in the time-averaged model. Second, once the oscillatory mode becomes stable, it soon becomes faster than the vertical mode. The passively stable flights mostly have their vertical flight mode as the slowest subsidence mode. This is different from the time-averaged mode, where the complex mode is always slowest. The second difference depends on the frequency of the vertical flight mode, which in turn depends on the choice of model parameters.

Both our models suggest that, once the wing attachment point is sufficiently high

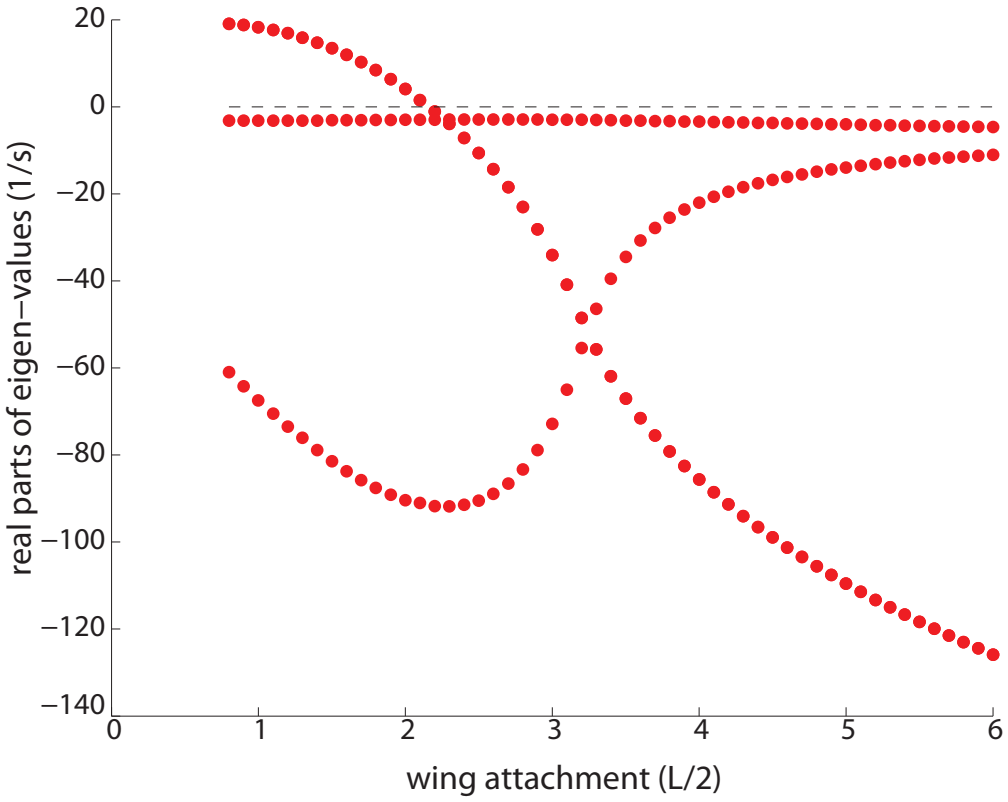

Figure 4.8: Eigenvalues of periodic flights versus wing attachment, h, measured in half body length, $\frac{L}{2}$. Only real parts are plotted to show flight stability. Flight is unstable for $h < 2.2$ and becomes passively stable for $h \geq 2.2$.

above the center of mass, the flight is passively stable and no longer needs active control. However, after we examine the periodic flights, we find that the vertical velocity decrease monotonically with the increase in the height of wing hinges. Eventually, the flight becomes a stable descent, rather than a stable hovering. In Figure 4.9, we plot the averaged vertical velocity as a function of wing attachment. At $h = 2.2$, the vertical flight is around -12 cm/s. With the increase in h, the descending speed increases, because the body oscillates with larger amplitude.

In our research, we find that the elevation of the wing hinges has two effects, one favorable to the flight stability and the other unfavorable to the vertical lift. The favorable effect is related to the rotational counter-torque that is approximately proportional to h^2.

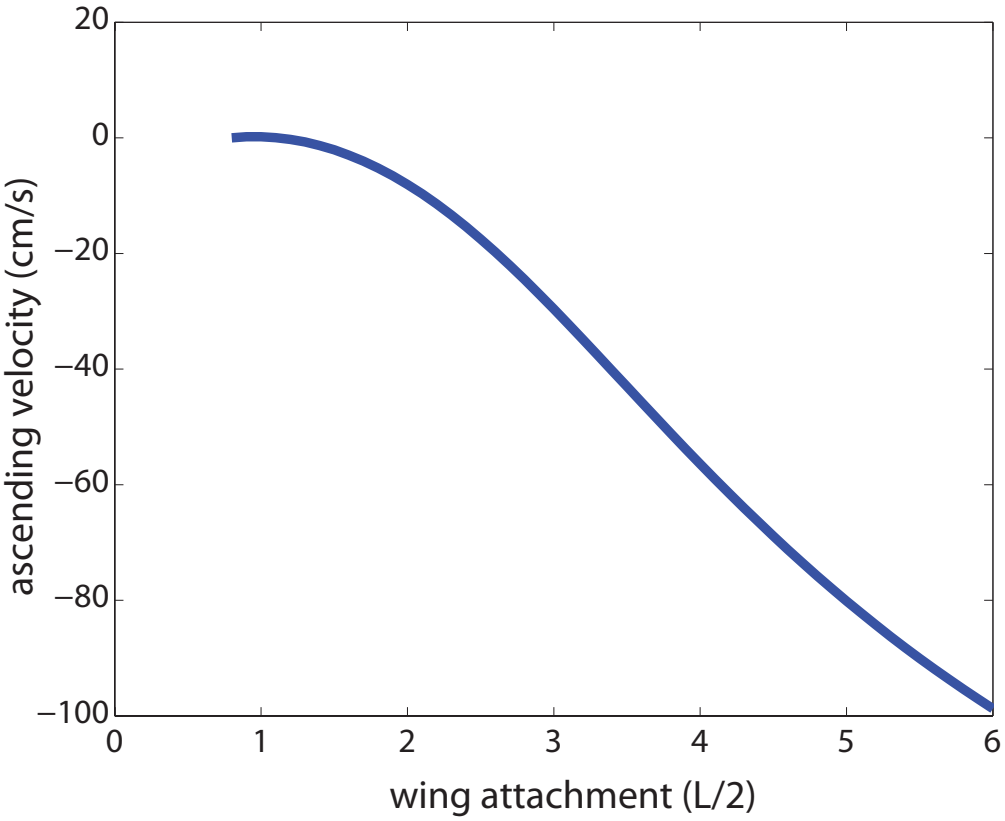

Figure 4.9: Ascending velocity of periodic flights versus wing attachment, h, measured in half body length, $\frac{L}{2}$. The flight is hovering for h around 1 and gradually becomes descending as h increases. At the critical value, $h = 2.2$, flight becomes passively stable and descends with a speed around 12 cm/s. This stable descent is not captured by the time-averaged model.

Increasing h thus adds damping to the body rotation and enhances the flight stability. On the other hand, when wings are farther away from the center of mass, the periodic drag on the wings drives the body to oscillate with larger amplitude, due to a longer force arm. The second effect is unfavorable in that it reduces the averaged vertical lift and causes the fly to descend.

To choose an optimal wing attachment point, the needs for stability and for lift generation should be balanced. It is beneficial to have wings high above the center of mass so that the flight become passively stable, or at least less unstable. As revealed by our

analysis in the 3D dynamic flight model, passively stable flight is limited by the slowest subsidence model, the vertical flight mode, once $h \geq 2.3$. Moving the wings higher than $h = 2.3$ does not enhance the system stability but only adds to the body oscillation. For passively stable flight, we thus suspect that an h value around $2.2 \sim 2.3$ may be an optimal choice for the design. This is approximately a body length above the center of mass. We understand that this estimate of an optimal wing attachment point may depend on our choice of model parameters.

One way of balancing the descending velocity at $h = 2.2$ is to increase the wing stroke amplitude. A larger lift may decelerate the body decent and restore the body to hovering. However, we fail to obtain a stable hovering in this way, because flight becomes unstable again after we increase the stroke amplitude. We find that the stroke amplitude also affects the flight stability, and that the flight becomes more unstable with the increase in the stroke amplitude. The relation between the flight stability and the stroke amplitude is the topic in the next chapter.

4.3 Conclusion

We studied the possibility of achieving a passively stable hovering flight by shifting the wing attach point upwards away from the body center of mass. Our rationale is based on the similarity between the counter torques generated by damping sails and by flapping wings during body rotation. To answer this question about the possibility, we first implemented a time-averaged model where aerodynamic forces are averaged over each wing-beat. We reached two conclusions that were independent of model parameters: (1) flapping flight was always unstable, when wings were attached below the center of mass; and (2) flapping flight was intrinsically unstable, when the damping force and torque on

the body are negligible. In a numerical simulation, we demonstrated that flapping flight might be passively stable, when wings were attached above a critical height over the center of mass.

To compare with those results, we studied the effect of the wing attach point on flight stability in our 3D dynamic flight model. We introduced our methods of finding periodic flights in the model and of analyzing the linear stability of associated Poincaré maps. The results from the 3D dynamic flight model partially agreed with those from the time-averaged model in that flapping flight became passively stable when wing hinges were sufficient high above the center of mass. The 3D dynamic flight model also showed that the passively stable flight was descending flight but not hovering, due to the increased body oscillation and reduced vertical lift. This was not captured by the time-averaged model, signifying the importance of the instantaneous coupling between the body and the wings. We pointed out that an optimal choice of wing attachment point ought to be based on the balance between the need for stability and the need for lift.

CHAPTER 5

Dynamic Stability and Body-pitch Control for an Ascending Insect

We have analyzed the flight stability and the body-pitch control for the model insect at hovering. A natural question is how insects stabilize other types of flight, such as ascending flight. In this chapter, we investigate the performance of our proposed controller for hovering, when the model insect ascends. We test whether the same controller works well for ascending flight at different flight speeds.

In principle, to elicit a body translational velocity along the vertical direction, the insect can modulate either wing stroke amplitude, or wing frequency, or wing angle of attack, or a combination of these three parameters. Here we focus on the wing stroke amplitude. Increasing the wing stroke amplitude increases the aerodynamic lift and causes the insect to accelerate upwards until it reaches a steady state ascending velocity.

We first simulate free flight by raising the wing stroke amplitude above a threshold value at which the insect hovers. Without active control for body-pitch, we show that ascending flight is not stable, and the insect eventually tumbles and descends, as a result of the dynamic coupling between the body-pitch rotation and forward motion. We then quantify the stability of periodic flights with different vertical velocities. We note that a vertical flight can be passively stable only when the insect descends with a substantial velocity. When the insect ascends, however, the flight is always unstable and becomes more so as the ascending velocity increases. We thus conclude that faster ascending flight may be more difficult to stabilize than slower ascending flight and hovering.

To stabilize ascending flight, we adopt the same controller we designed for hovering flight. We use the same control gains, and choose the controller time scales $T_s = 1$, $T_{d,1} = 2$, and $T_{d,2} = 0.2$, which are inferred from the phase diagram of controller per-

formance. After we implement the controller, the model insect ascends stably, when ascending speed does not exceed 10 cm/s. Once the ascending speed is above this critical value, ascending flight becomes more and more unstable, which is manifested in the increasing oscillation amplitude of body-pitch. The model insect becomes unstable and tumbles and descends, after we increase the wing stroke amplitude above 72°.

The maximal speed of ascending in our simulation is smaller than what has been observed for fruit flies in laboratory, i.e. around 35 cm/s. One possible reason is that fruit flies utilize different control gains or nonlinear control in adapting to different ascending velocities. To reveal the nature of control schemes used by fruit flies, further work is needed to record the wing stroke patterns during ascending flight with different ascending speeds.

Finally, we examine the linear relation between the ascending velocity and the wing velocity in the time-averaged model. We identify a one-dimensional vertical flight that corresponds to a flight restricted to a vertical line. This vertical flight is stable with typical parameters for fruit flies. We show that terminal speed of the vertical flight is an implicit function of wing stroke amplitude, or equivalently, the wing velocity. Using numerical simulation, we show that vertical flight speed depends linearly on wing velocity over a typical range of ascending speeds for fruit flies.

5.1 Uncontrolled Flight Simulation of Ascending Flight

To fly upwards, fruit flies may alter parameters of their wing motion, such as the wingbeat frequency, the wing stroke amplitude, and the wing angle of attack. We do not choose the wing angle of attack because it is at most weakly correlated with the ascending velocity of fruit flies [55]. On the other hand, the ascending velocity is strongly

correlated with the wing velocity. Although both the wing-beat frequency and the wing stroke amplitude can influence the wing velocity, we do not choose the wing-beat frequency because it is usually fixed at the resonant frequency of the wing-root structure [27, 58]. On the other hand, flying insects use direct steering muscles to modulate their wing stroke amplitude [59], which is the parameter we use to elicit ascending flight in this section.

The model insect tumbles and descends in the uncontrolled flight simulation and hovers in the controlled flight simulation (section 3.3). In steady state, our proposed controller stabilizes the body-pitch oscillation within $\pm 1^\circ$. On average, the vertical lift is almost equal to the body weight at the wing stroke amplitude of 63.1°. We study whether the insect ascends stably with stroke amplitudes above the threshold value of 63.1°.

We simulate a number of free flights without active control of body attitudes and show two cases with stroke amplitudes of $\phi_m = 64^\circ$ and $\phi_m = 68^\circ$ (Figure 5.1). These amplitudes are, respectively, about 1° and 7° larger than the critical stroke amplitude. Both flights begin with the insect stationary and at upright, and we observe unstable flight similar to the uncontrolled flight simulation (section 3.1). The body-pitch becomes unstable after a typical time of 50 wing-beats. The insect eventually tumbles and descends, instead of flying upwards.

5.2 Stability Analysis of Ascending Flight

We carry out a stability analysis for ascending flight, using the same method as described in the last chapter. By varying the wing stroke amplitude in the 3D dynamic flight model, we first search for periodic ascending flights with different ascending velocities. We then

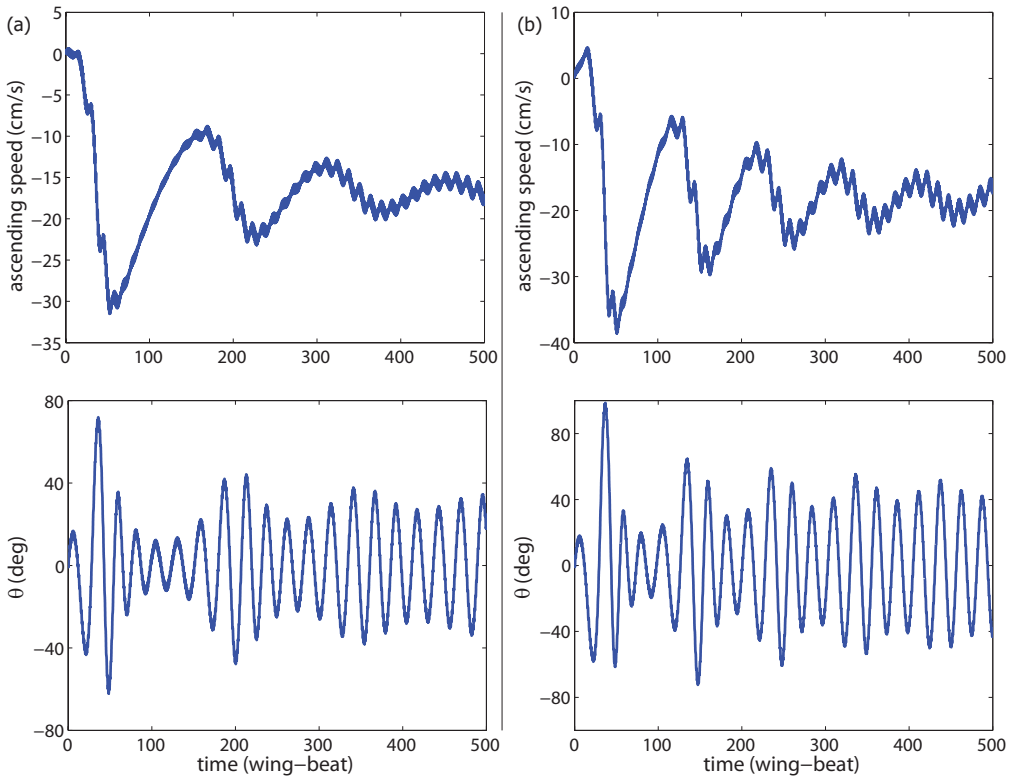

Figure 5.1: Ascending speed and body-pitch in uncontrolled ascending flight. (a) $\phi_m = 64°$. (b) $\phi_m = 68°$. Both flights are unstable in body-pitch.

quantify the stability of the periodic ascending flights by linear stability analysis of the associated Poincaré maps.

Figure 5.2 shows the real parts of eigenvalues associated with the periodic flights, when the wing stroke amplitude (ϕ_m) is varied between 55° and 75°, with a constant increment of 0.1°. The induced ascending speed is between −51.2 cm/s and 37.4 cm/s, where negative speeds correspond to descending flights. The hovering flight ($v_z \simeq 0$) is reached at $\phi_m = 63.1°$, the same threshold value. The largest real part increases with the increase in ϕ_m, which suggests that the periodic ascending flights become more unstable, and potentially more difficult to control, at higher ascending speeds. It is interesting to note that most of the flights are unstable, except for those fast descending flights from the left panel in the figure.

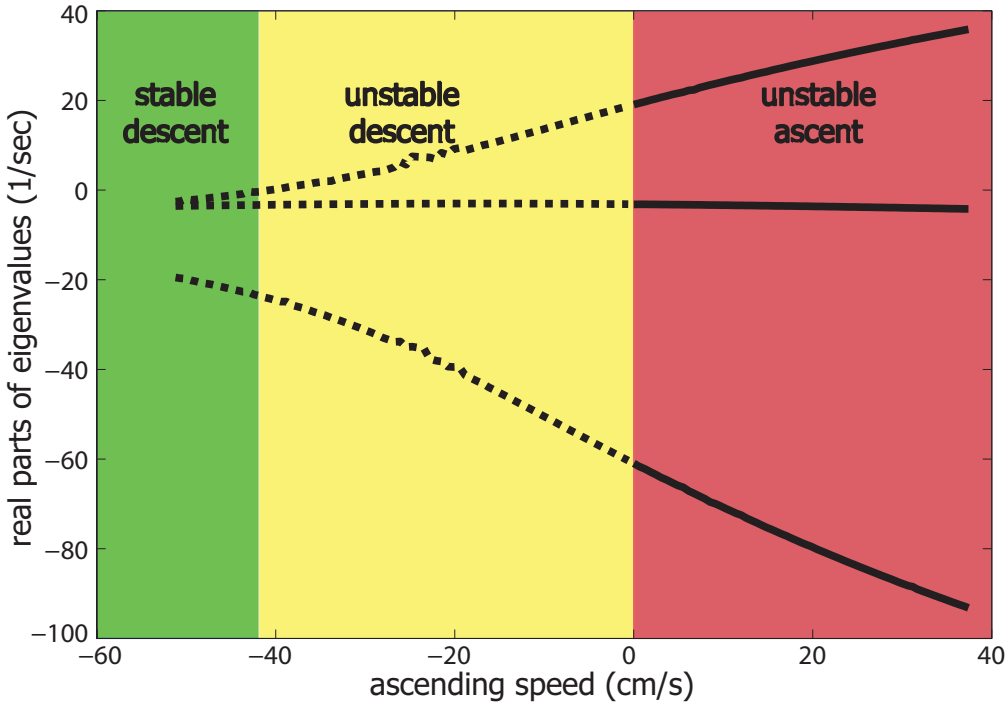

Figure 5.2: Real parts of eigenvalues for periodic flights with different ascending velocities. Wing stroke amplitude varies between 55 and 75 deg., and the induced ascending speed ranges from −51.2 cm/s to 37.4 cm/s. The increase in the largest eigenvalue reveals a more unstable mode in flight with faster ascending speed.

5.3 Controller Performance in Ascending Flight

When studying the body-pitch control for a hovering insect, we devised a discrete-sampling, time-delayed, linear controller that modulated the center position of wing strokes based on measurements of body-pitch attitude and body-pitching rate. The controller stabilized the hovering flight with a wing stroke amplitude of 63.1°. There were three time scales in our control scheme. The actuation delay was fixed at 0.2 wing-beat. Based on the 2D phase diagram of controller performance, we inferred that fruit flies relied on a sampling interval of one wing-beat and took control actions with a delay of around two wing-beats.

In this section, we further study the body-pitch control for ascending flight, using our 3D dynamic flight model. We adopt the same control algorithm used for the body-pitch control at hovering. To test whether the same controller works for insects in ascending flight, we retain the control gains and choose $T_s = 1$ and $T_{d,1} = 2$. $T_{d,2} = 0.2$ is fixed as before.

5.3.1 Terminal Ascending Velocity and Body-pitch Oscillation in Controlled Ascending Flight

We increase the wing stroke amplitude to elicit the vertical flight speed. The model insect starts from stationary initial conditions and an upright body orientation. For each chosen wing stroke amplitude, we simulate a free flight for 1000 wing-beats, a sequence long enough for us to examine flight stability and to evaluate the terminal ascending speed and body attitude. In each simulation, either well controlled or poorly controlled, the flight eventually settles down to a periodic oscillation in body-pitch attitude, with a small amplitude in a well controlled flight and a large amplitude in a poorly controlled flight.

We use the last 10% of the simulation, i.e. the last 100 wing-beats in the simulation, to quantify the behavior of the flight in the terminal state. We compute both the mean and the standard deviation for the vertical flight velocity and the body attitude. The mean vertical flight speed provides an estimate of the terminal ascending speed, v_∞. The standard deviation of the vertical flight velocity is positively related to the amplitude of body oscillation, or the standard deviation of body attitude, $\Delta\theta_\infty$. The mean body attitude provide an estimate of the direction of the flight.

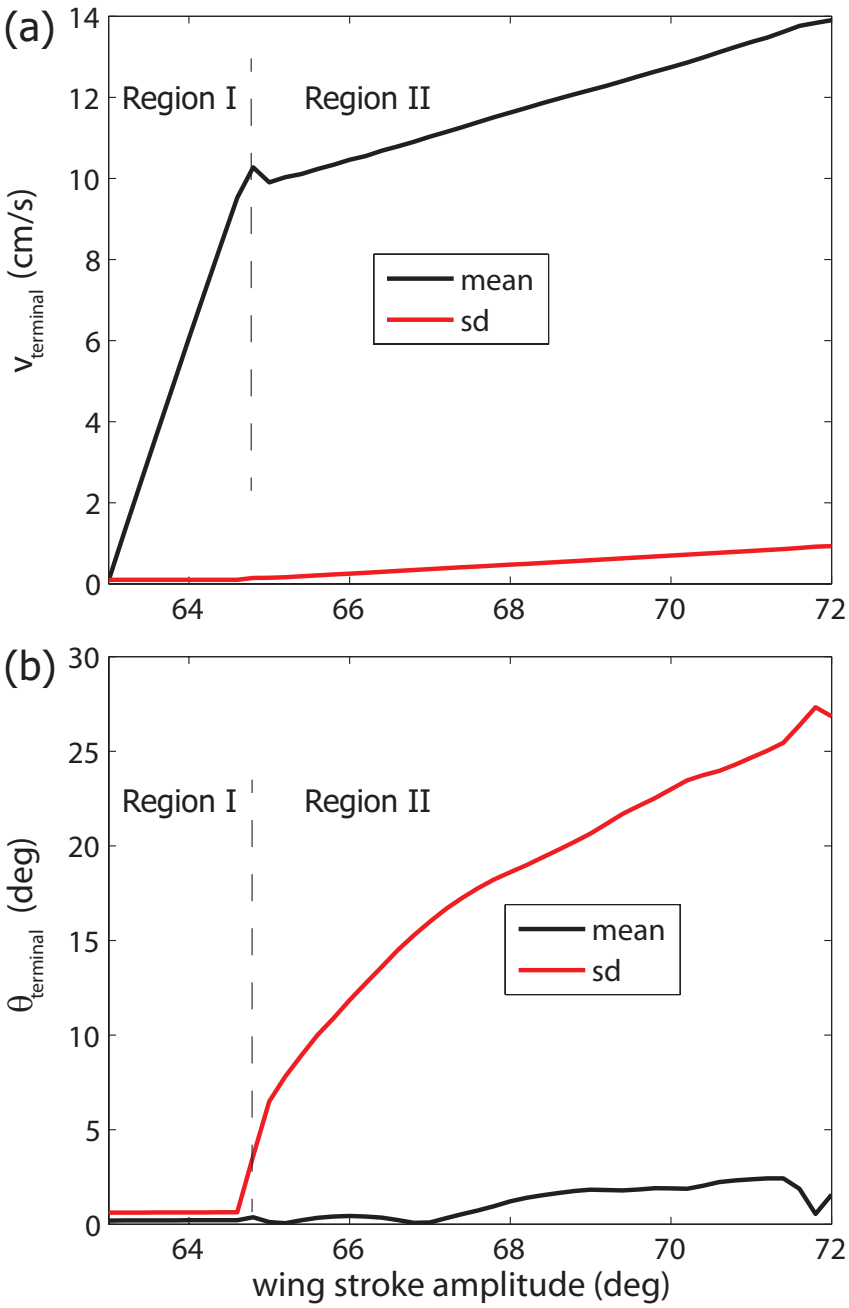

Figure 5.3: Terminal ascending velocity and body-pitch in 3D dynamic flight model. (black) Mean values. (red) Standard deviations, or oscillation amplitudes.

We plot the mean and the standard deviation of the vertical flight speed versus the wing stroke amplitude in Figure 5.3(a). The wing stroke amplitude is varied between

63° and 72°, with a constant increment of 0.2°. The standard deviation increases with the increase in the stroke amplitude, but its variation is not as noticeable as that of the terminal ascending speed. We also note that the terminal ascending speed is divided into two regions separated by a critical value at $\phi_{m,c} = 64.8°$. The ascending flight speed is around 10 cm/s at the transition between the two regions. In each region, the terminal ascending speed increases almost linearly with the stroke amplitude, but the slopes are different. The slope is $5.8 cm/(s \cdot DEG)$ in region I and $0.58 cm/(s \cdot DEG)$ in region II. The slope in each region characterizes the sensitivity of terminal ascending speed in response to the increase in the stroke amplitude. It also quantifies the efficiency of this specific ascending maneuver, because a steep slope means less increase in the stroke amplitude to invoke the same ascending speed. Therefore, this ascending maneuver is only 10% as efficient in region II as in region I.

The reduction in the efficiency is explained by an examination of the mean value and the standard deviation of the body attitude (Figure 5.3(b)). In this plot, the variation in the mean body-pitch attitude is not as evident as that in the amplitude of the terminal body oscillation. The body oscillation is approximately symmetrical about the upright orientation. The amplitude of the body oscillation also displays a transition between two regions, corresponding to the regions in the plot of the terminal ascending velocity. In region I, the flight is well controlled, as manifested by the small oscillation amplitude. In region II, the oscillation amplitude increases with the stroke amplitude, and the flight gradually becomes poorly controlled. Therefore, increasing the stroke amplitude in region II has two effects: a larger body oscillation amplitude, and a larger aerodynamic lift. The vertical lift on average is determined by the competition between the two effects. Whether the terminal ascending speed increases or decreases with the stroke amplitude depends on which effect is more important. The kink in Figure 5.3(a) shows that the transition between the two regions starts with the first effect more important, but the

second effect soon becomes dominant and leads to the increase in the ascending speed with the wing stroke amplitude. In comparison, the increase of the stroke amplitude in region I only increases the aerodynamic lift and leads to faster increase in ascending speed.

If we increase the stroke amplitude above 72°, flight becomes unstable. This agrees with what we learn from the stability analysis that flight becomes more unstable with faster ascending velocity.

5.3.2 Two Examples of Controlled Ascending Flight Simulation

Figure 5.4 shows two typical flight sequences from Region I and II, respectively. $\phi_m = 64°$ in Figure 5.3(a), and the flight is well controlled. The terminal ascending velocity has a relatively small fluctuation compared to its mean value after the transient, indicating nearly uniform ascent. The body-pitch amplitude (θ_b) shows a symmetric back-and-forth oscillation about the upright position (Figure 5.3(b)).

The amplitude of the oscillation depends sensitively on ϕ_m. $\phi_m = 68°$ in Figure 5.3(b), which is above the critical $\phi_{m,c} = 64.8°$, and the insect undergoes a large oscillation in body-pitch. The flight was stabilized for the first 100 wing-beat until the insect reaches about 20 cm/s. After that, the flight becomes poorly controlled, as seen in an increasing body-pitch oscillation and a reduced ascending speed.

In Figure 5.4(b), the model fly is able to fly upwards until the ascending velocity goes above 20 cm/s. At this speed, the controller no longer compensates for the body-pitch instability as well as it does in hovering. This causes the body attitude to start oscillating, and the oscillation has once reached ±50°. Eventually, the fly settles with an

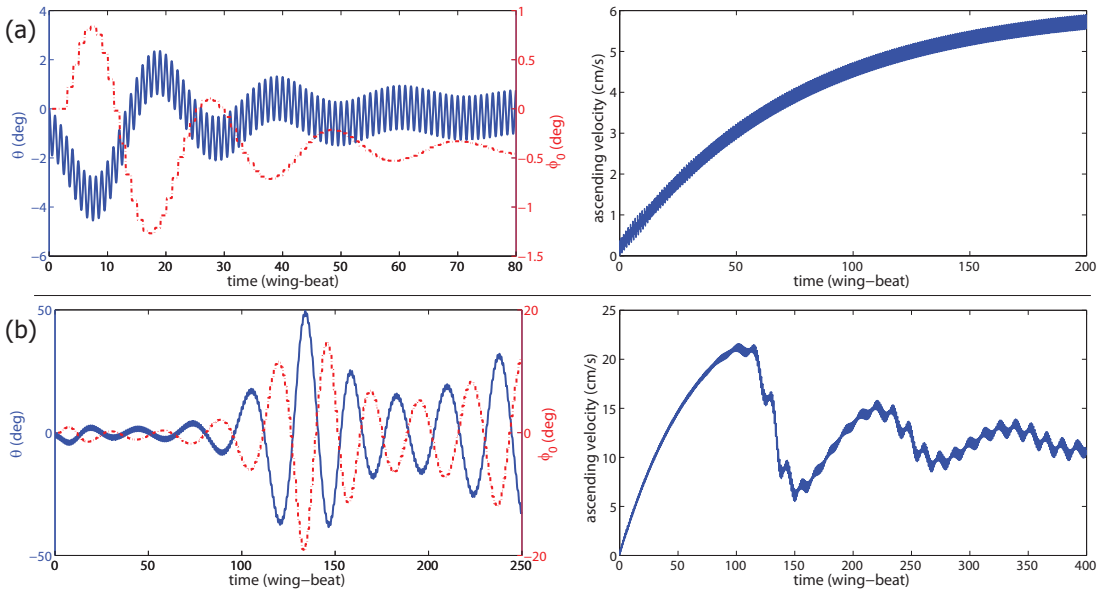

Figure 5.4: Vertical velocity and body-pitch attitude in controlled ascending flights. The insect body starts at rest and upright. (a) A well controlled flight from region I with $\phi_m = 64°$. Terminal ascending velocity is 6.1 cm/s, and terminal body-pitch oscillation amplitude is 0.8°. (b) A poorly controlled flight from region II with $\phi_m = 68°$. Terminal ascending velocity is 11.6 cm/s, and terminal body-pitch oscillation amplitude is 26.8°. The body-pitch becomes poorly controlled at approximately 100 wing-beats, where the body ascends with velocity around 20 cm/s.

ascending speed lower than what can be supported by the total lift force.

5.3.3 Discussion

The terminal velocity in the ascending flight reaches about 10 to 12 cm/s before flight becomes poorly controlled. This value is smaller than the maximal ascending speed of fruit flies observed in laboratory, which is typical around 35 cm/s. The wing stroke amplitude is above 80° at an ascending speed around 35 cm [55]. In those experiments, fruit flies are confined by the filming apparatus, and thus they may fly with even high ascending speed in wild space. Our model insect has not achieved this fast ascent, because the

body-pitch is poorly controlled for fast ascending flight, which has been predicted to be more unstable than hovering. Our results show that the controller designed for hovering flight only works well in controlling ascending flight slower than 10 to 12 cm/s.

One possibility is that fruit flies rely on different control algorithms at different ascending speeds. Because our controller is not adapted to the ascending speed, it may not be able to stabilize ascending flight as satisfactorily as living fruit flies. To resolve this puzzle, future research may record wing stroke patterns of fruit flies, or other flying insects, at different ascending speeds and analyze the wing modulation.

5.4 Ascending Speed versus Wing Velocity in Time-Averaged Model

We analyze the ascending flight using our time-averaged model and compare the results with those from the 3D dynamic flight model. To extract analytical results, we simplify the time-averaged model and restrict the flight to a vertical line. This results in a one-dimensional invariant set corresponding to the vertical flight whose speed depends on the wing velocity through an implicit function. For typical parameters of fruit flies, the flight is stable and reaches the terminal velocity without active control.

In the time-averaged model, we restrict the flight to a vertical line by imposing an initial condition $u(0) = \theta(0) = \omega(0) = 0$. This restriction leads to $\dot{u} = \dot{\theta} = \dot{\omega} = 0$, and thus $u(t) = \theta(t) = \omega(t) = 0$ for all time t. We thus find a one-dimensional invariant set where the only nontrivial variable is the vertical flight velocity. The one-dimensional flight dynamics in terms of v are

$$m\dot{v} = L\cos\beta - D\sin\beta - mg.$$

where L is the aerodynamic lift, D is the aerodynamic drag, m is the body mass, and g is

the gravitational constant. We calculate the aerodynamic forces using the classic airfoil theory [55]. The flight dynamics are

$$\dot{v} = \frac{W\sin\alpha - v\cos\alpha}{\lambda\sqrt{W^2+v^2}}[(2c_L W^2 + 2c_D v^2)\cos\alpha + (2c_L - 2c_D)Wv\sin\alpha] - 1, \quad (5.1)$$

for $v(0) = v_0$ where v_0 is the initial ascending velocity. Here we normalize the physical variables using a length scale of $\bar{c} \sim 1$ mm and a time scale of $\sqrt{\bar{c}/g} \sim 10$ ms. The quotient of the two scales, 10 cm/s, is the velocity scale. $\lambda = \frac{m}{\rho_f \bar{c}^2 R}$. This model agrees with the result in [55].

The equilibrium ascending velocity, v_∞, is given by the fixed point of the flight dynamic equation,

$$0 = \frac{W\sin\alpha - v_\infty\cos\alpha}{\lambda\sqrt{W^2+v_\infty^2}}[(2c_L W^2 + 2c_D v_\infty^2)\cos\alpha + (2c_L - 2c_D)Wv_\infty\sin\alpha] - 1 \quad (5.2)$$

The equation establishes an implicit function between v_∞ and the wing velocity W. We reason that this function should be monotonically increasing, because increasing the wing velocity engenders larger aerodynamic lift, which can only be balanced by higher ascending speed.

This equation does not have a closed-form solution. We may find approximate solutions through a Taylor expansion. If we only keep the leading order terms in v_∞, we find the following approximate solution,

$$v_{\infty,\text{appr}} = \frac{c_L W^2 \sin 2\alpha - \lambda}{2W(c_L\cos 2\alpha + c_D \sin^2\alpha)}. \quad (5.3)$$

We try to keep both the linear and quadratic terms in v_∞ and use the quadratic formula to solve the expanded equation,

$$[(2c_D - c_L)W\sin 2\alpha - \frac{\lambda}{2W}]v^2 - W^2[2c_L\cos 2\alpha + c_D(1-\cos 2\alpha)]v + W[c_L W^2\sin 2\alpha - \lambda] = 0 \quad (5.4)$$

However, this equation has no real roots for the values of W studied here.

We may also solve the equation numerically, using parameters for fruit flies. Typical wing velocity of fruit flies is around 2 m/s. In Figure 5.5, we display the numerical solution of the terminal ascending speed as the wing velocity varies between 1.8 and 2.2 m/s. We overlay the first order approximated solution, which does not exhibit good agreement with the precise solution over the range of ascending velocity. The nearly linear relation between the wing velocity and the ascending velocity agrees with what we observe in the 3D dynamic flight model, although we have not implemented any control in the time-averaged model. The flight reaches 20 cm/s for a 5% increase in the wing velocity. This may be converted to a slope of 6.3 cm/(s· DEG), which is very close to what we have in the region I from the 3D dynamic flight simulation.

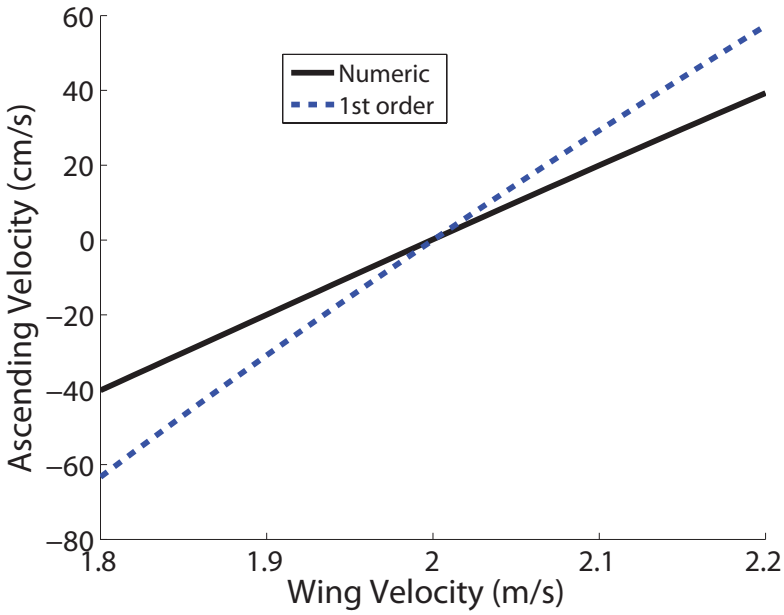

Figure 5.5: Terminal ascending velocity solved from both the vertical 1D model and a linear approximation. v and W are dimensionless with velocity scale of 10 cm/s. Parameters used are: $c_D = 1$, $c_L = 1.5$, $\lambda = 700$, $\alpha = 45\,^\circ$. The two curves separate except for the point where $v = 0$.

To assess the stability of the equilibrium flight speed, we carry out a perturbation

analysis along v-direction. Let δv be the perturbation to the ascending velocity. The perturbed dynamics are,

$$\delta\dot{v} = f(v_\infty + \delta v) = \left(\frac{\partial f}{\partial v}(v_\infty)\right) \cdot \Delta v = -J\Delta v \tag{5.5}$$

where $J > 0$ for the W values studied here. The one-dimensional vertical flight is stable.

$1/J$ is an estimate of the decay time of the deviation from the equilibrium ascending speed. Figure 5.6 shows the decay time, measured in wing-beats, as a function of the terminal ascending velocity. It ranges between 50 to 70 wing-beats and equals 60 wing-beats at hovering, which is on par with the time of body saccades around 50 wing-beats [22]. In ascending flight where $v_\infty > 0$, the decay time decreases with the terminal ascending speed.

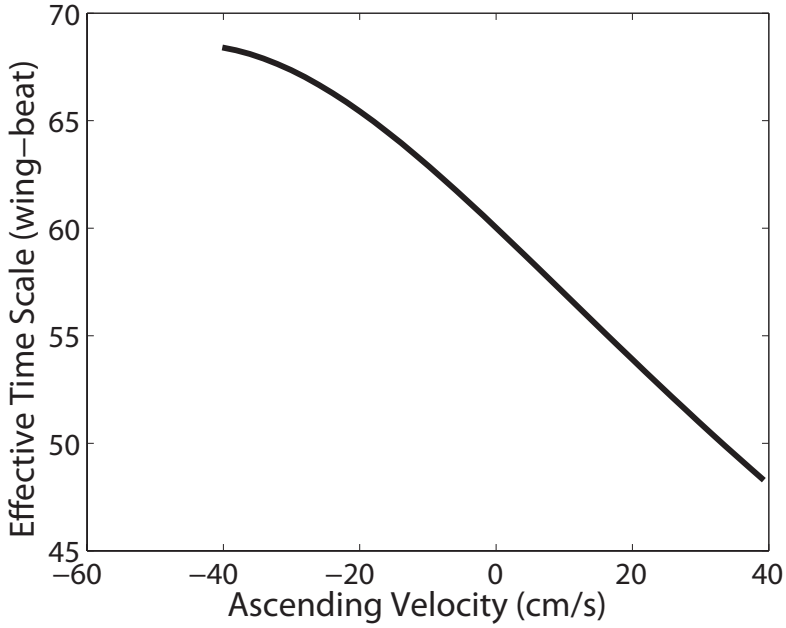

Figure 5.6: The decay time (τ) as a function of equilibrium ascending velocity (v_{eq}). For $v_{eq} > 0$, τ strictly decreases, which reflects the fact that the restoring force is also positively correlated to v_{eq}. At hovering, the decay time is about 60 wing beats.

5.5 Conclusion

We studied ascending flight by increasing the wing stroke amplitude. We first simulated uncontrolled free flight and identified similar body-pitch instability as observed in the simulation of hovering flight. The instability was due to the dynamic coupling between the body-pitch rotation and the forward motion. We further quantified the instability of ascending flight with different ascending speeds and found that ascending flight became more unstable at higher speed.

To stabilize the body-pitch in ascending flight, we adopted the same controller we designed for hovering flight. We retained the control gains and set controller time scales to what we inferred from the 2D diagram of controller performance. The controller stabilized flight well in ascending flight with speed below 10 cm/s, where the ascending speed increased linearly with the stroke amplitude. For faster ascending flight, we noticed poor performance of the controller and an increasing oscillation amplitude in the body-pitch. Once we increased the wing stroke amplitude over 72°, the flight became unstable, and the model insect tumbled and descended, instead of flying upwards.

In laboratory, the maximal ascending speed of fruit flies was observed to be around 35 cm/s, higher than what our 3D dynamic flight model predicted. One possibility was that fruit flies adapted their body-pitch control strategy to the flight speed. Future research might record the wing stroke patters of fruit flies in both slow and fast ascending flights and compare their stabilization strategy.

Finally, we established a linear relation between the ascending velocity and the wing velocity in our time-averaged model, by restricting the flight to a vertical line. This restricted vertical flight was stable. The linear slope we inferred from the time-averaged model was very close to what we learned from the 3D dynamic flight model

BIBLIOGRAPHY

[1] Wood RJ. The first takeoff of a bioloigically inspired at-scale robotic insect. *IEEE Trans. Robotics*, 24:341–347, 2008.

[2] Sun M and Xiong Y. Dynamic flight stability of a hovering bumblebee. *J. Exp. Biol.*, 208:447–459, 2005.

[3] Sun M, Wang JK, and Xiong Y. Dynamic flight stability of hovering insects. *Acta Mech. Sin.*, 23:231–246, 2007.

[4] Pringle JWS. The gyroscopic mechanism of the haltere of diptera. *Phil. Trans. R. Soc. B.*, 233(602):347–384, 1948.

[5] Ristroph L, Ristroph G, Morozova S, Bergou AJ, Chang S, Guckenheimer JM, Wang ZJ, and Cohen I. Active and passive stabilization of body pitch in insect flight. *J. R. Soc. Interface*, 10(85):20130237, 2013.

[6] Götz KG, Hengstenberg B, and Biesinger R. Optomotor control of wing beat and body posture in drosophila. *Biol. Cybern.*, 35:101–112, 1979.

[7] Ellington CP. The aerodynamics of hovering insect flight. iii. kinematics. *Phil. Trans. R. Soc. B.*, 305:41–78, 1984.

[8] Heisenberg M and Wolf R. The sensory-motor link in motion dependent flight control of flies. *Rev. Oculomot. Res.*, 5:265–283, 1993.

[9] Dudley R. *The Biomechanics of Insect Flight: Form, Function, Evolution*. Princeton: Princeton University Press, 2000.

[10] Dickinson MH, Farley CT, Full RJ, Koehl MAR, Kram R, and Lehman S. How animals move: An integrative view. *Science*, 288:100–106, 2000.

[11] Taylor GK and Krapp HG. Sensory systems and flight stability: what do insects measure and why. *Advances in Insect Physiology*, 34:231–316, 2007.

[12] Bergou AJ, Ristroph L, Guckenheimer JM, Cohen I, and Wang ZJ. Fruit flies modulate passive wing pitching to generate in-flight turns. *Phys. Rev. Lett.*, 104:148101, 2010.

[13] Ristroph L, Bergou AJ, Ristroph G, Coumes K, Berman G, Guckenheimer JM, Wang ZJ, and Cohen I. Discovering the flight autostabilizer of fruit flies by inducing aerial stumbles. *PNAS*, 107(11):4820–4824, 2010.

[14] Cheng B, Deng X, and Hedrick TL. The mechanics and control of pitching manoeuvres in a freely flying hawkmoth manduca sexta. *J. Exp. Biol.*, 214:4092–4106, 2011.

[15] Reichardt W and Poggio T. Visual control of orientation behavior in the fly i. a quantitative analysis. *Q. Rev. Biophys.*, 9(3):311–375, 1976.

[16] Tammero LF and Dickinson MH. Collision-avoidance and landing responses are mediated by separate pathways in the fruit fly, drosophila melanogaster. *J. Exp. Biol.*, 205:2785–2798, 2002.

[17] Sherman A and Dickinson MH. A comparison of visual and haltere-mediated equilibrium reflexes in the fruit fly drosophila melanogaster. *J. Exp. Biol.*, 206:295–302, 2003.

[18] Zanker JM. The wingbeat of *drosophila melanogaster*. iii. control. *Phil. Trans. R. Soc. Lond. B*, 327:45–64, 1990.

[19] Hollick FSJ. The flight of the dipterous fly muscina stabulans fallen. *Phil. Trans. R. Soc. B.*, 230:357–390, 1940.

[20] Dudley R and Ellington P. Mechanics of forward flight in bumblebees, part 1. kinematics and morphology. *J. Exp. Biol.*, 148:19–52, 1990.

[21] Combes SA and Dudley R. Turbulence-driven instabilities limit insect flight performance. *PNAS*, 106(22):9105–9108, 2009.

[22] Fry SN, Sayaman R, and Dickinson MH. The aerodynamics of free-flight maneuvers in drosophila. *Science*, 300:495–498, 2003.

[23] Fry SN, Sayaman R, and Dickinson MH. The aerodynamics of hovering flight in drosophila. *J. Exp. Biol.*, 208:2303–2318, 2005.

[24] Ristroph L, Berman G, Bergou A, Wang ZJ, and Cohen I. Automated hull reconstruction motion tracking applied to sideways maneuvers of free-flying insects. *J. Exp. Biol.*, 212:1324–1335, 2009.

[25] Ristroph L, Bergou AJ, Guckenheimer JM, Wang ZJ, and Cohen I. Paddling mode of forward flight in insects. *Phys. Rev. Lett.*, 106:178193, 2011.

[26] Fontaine EI, Zabala F, Dickinson MH, and Burdick JW. Wing and body motion during flight initiation in drosophila revealed by automated visual tracking. *J. Exp. Biol.*, 212:1307–1323, 2009.

[27] Ma KY, Chirarattananon P, Fuller SB, and Wood RJ. Controlled flight of a biologically inspired, insect-scale robot. *Science*, 340:603–607, 2013.

[28] Faruque I and Humbert JS. Dipteran insect flight dynamics. part1: Longitudinal motion about hover. *J. Theor. Biol.*, 264:538–552, 2010.

[29] Wu JH and Sun M. Floquet stability analysis of the longitudinal dynamics of two hovering model insects. *J. R. Soc. Inter.*, 9(74):2033–46, 2012.

[30] Zhang Y and Sun M. Dynamic ight stability of a hovering model insect: Lateral motion. *Acta Mech. Sin.*, 26:175190, 2009.

[31] Faruque I and Humbert JS. Dipteran insect ight dynamics. part 2: Lateral-directional motion about hover. *J. Theor. Biol.*, 265:306313, 2010.

[32] Etkin B. *Dynamics of flight stability and control*. John Wiley and Sons, Inc., 1983.

[33] Taylor GK and Thomas ALR. Dynamic flight stability in the desert locust schistocerca gregaria. *J. Exp. Biol.*, 206:2803–2829, 2003.

[34] Wu JH, Zhang YL, and Sun M. Hovering of model insects: simulation by coupling equations of motion with navier-stokes equations. *J. Exp. Biol.*, 212:3313–3329, 2009.

[35] Sun M and Wang JK. Flight stabilization control of a hovering model insect. *J. Exp. Biol.*, 210:2714–2722, 2007.

[36] Goldstein H. *Classical mechanics*. Addison-Wesley Publishing Company., 1980.

[37] Featherstone R. *Rigid body dynamics algorithms*. Springer, 2008.

[38] Dickson WB, Straw AD, and Dickinson MH. Integrative model of drosophila flight. *AIAA J.*, 46(9):2150–2164, 2008.

[39] Udwadia FE and Kalaba RE. *Analytical dynamics: a new approach*. Cambridge University Press, 1996.

[40] Andersen A, Pesavento U, and Wang ZJ. Unsteady aerodynamics of fluttering and tumbling plates. *J. Fluid Mech.*, 541:65–90, 2005.

[41] Pesavento U and Wang ZJ. Falling paper: Navier-stokes solutions, model of fluid forces, and center of mass elevation. *Phys. Rev. Lett.*, 93(14):144501, 2004.

[42] Andersen A, Pesavento U, and Wang ZJ. Unsteady aerodynamics of fluttering and tumbling plates. *J. Fluid Mech.*, 541:65–90, 2005.

[43] Tuckerman LB. Inertia factors of ellipsoids for use in airship design. *Report National Advisory Committee for Aeronautics*, 210:62–67, 1926.

[44] Bergou AJ. A quantitative analysis of wing pitching in insect flight. Ph.D. Thesis. Cornell University. 2009.

[45] Berman GJ and Wang ZJ. Energy-minimizing kinematics in hovering insect flight. *J. Fluid Mech.*, 582:153–167, 2007.

[46] Trimarchi JR and Murphey RK. The shaking-b2 mutation disrupts electrical synapses in a flight circuit in adult drosophila. *J. Neurosci.*, 17:47004712, 1997.

[47] Heide G. Neural mechanisms of flight control in diptera. *BIONA-report*, 2:35–52, 1983.

[48] Fayyazuddin A and Dickinson MH. Haltere afferents provide direct, electronic, input to steering motor neuron in the blowfly, *Calliphora*. *J. Neurosci.*, pages 5225–5232, 1996.

[49] Fayyazuddin A and Dickinson MH. Convergent mechanosensory input structures the firing phase of a steering motor neuron in the blowfly, *Calliphora*. *J. Neurophysiol.*, 82:1916–1926, 1999.

[50] Heide G and Götz KG. Optomotor control of course and altitude in drosophila melanogaster is correlated with distinct activities of at least three pairs of flight steering muscles. *J. Exp. Biol.*, 199:17111726, 1996.

[51] van Breugel F, Teoh ZE, and Lipson H. *A passively stable hovering flapping micro-air vehicle*. Springer, 2009.

[52] Richter C and Lipson H. Untethered hovering flapping flight of a 3d-printed mechanical insect. *Artific Life*, 17:7386, 2011.

[53] Cheng B, Fry S, Huang Q, and Deng X. Aerodynamic damping during rapid ight maneuvers in the fruit y drosophila. *J. Exp. Biol.*, 213:602612, 2009.

[54] Hedrick TL, Cheng B, and Deng X. Wingbeat time and the scaling of passive rotational damping in apping ight. *Science*, 324:252255, 2009.

[55] Berman GJ. Optimization, control, and flies: Quantitative studies of insect fligh. Ph.D. Thesis. Cornell University. 2009.

[56] Ogata K. *Modern Control Engineering*. Prentice Hall, 5 edition, 2009.

[57] Dietl JM and Garcia E. Stability in ornithopter longitudinal flight dynamics. *J. Guidance, Control, and Dynamics*, 31(4):1157–1162, 2008.

[58] Perez-Arancibia NO, Ma KY, Galloway KC, Greenberg JD, and Wood RJ. First controlled vertical flight of a biologically inspired microrobot. *Bioinsp. Biomim.*, page 036009, 2011.

[59] Lehmann FO and Dickinson MH. The control of wing kinematics and flight forces in fruit flies. *J. Exp. Biol.*, 201:385–401, 1998.

[60] Chang S and Wang ZJ. Insects in Free Flight: Simulation, Dynamic Instability, and a Prediction for the Critical Sensing Rate for Flight Stabilization. *Proc. Natl Acad. Sci. USA*, in review.